

Distilling Diffusion Models to Efficient 3D LiDAR Scene Completion

Shengyuan Zhang¹ An Zhao¹ Ling Yang³ Zejian Li^{2,*} Chenye Meng¹
 Haoran Xu⁴ Tianrun Chen¹ AnYang Wei⁴ Perry Pengyun GU⁴ Lingyun Sun¹

¹ College of Computer Science and Technology, Zhejiang University ² School of Software Technology, Zhejiang University

³ Peking University ⁴ Zhejiang Green Zhixing Technology co., ltd

^{1,2}{zhangshengyuan, zhaoan040113, zejianlee, mengcy, tianrun.chen, sunly}@zju.edu.cn

³{yangling0818}@163.com ⁴{Haoran.Xu5, weianyang, gupengyun}@geely.com *Corresponding author

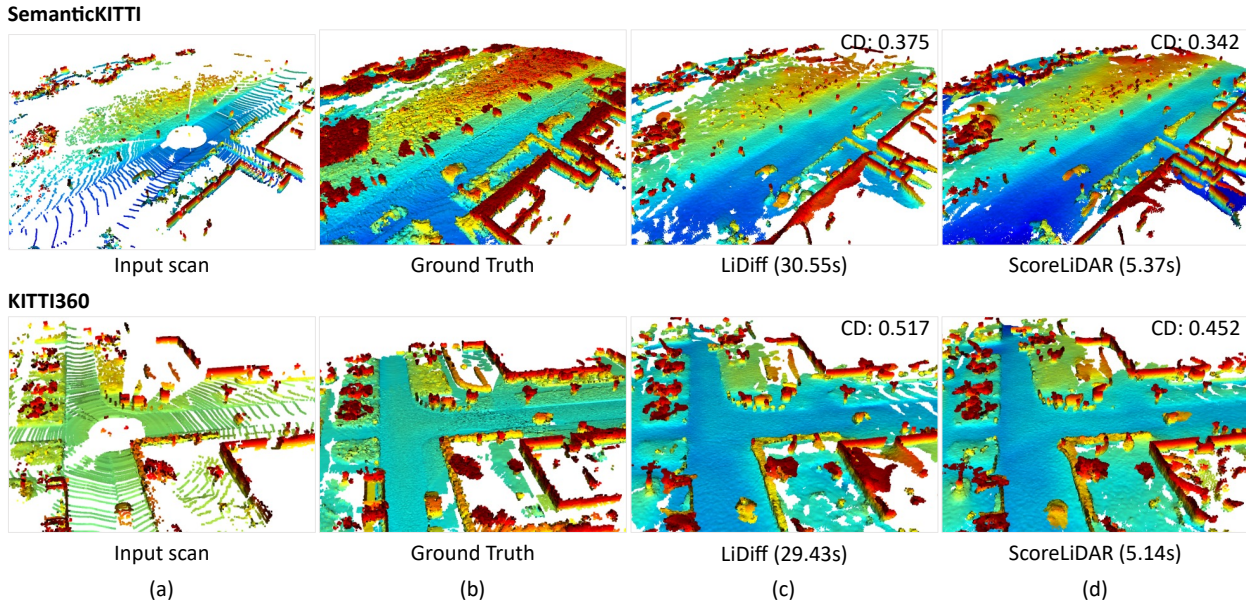


Figure 1. A demonstration of the LiDAR scene completion examples. Given a sparse LiDAR scan in (a), the model aims to recover the ground-truth dense scene as in (b). In these examples, scans are from SemanticKITTI [1] and KITTI360 [20] dataset. In both cases, LiDiff [28], a SOTA LiDAR scene completion method, requires about 30 seconds as in (c). In comparison, our proposed ScoreLiDAR takes only about 5 seconds in (d), achieving over 5x speedup with improved completion quality indicated by lower Chamfer Distance (CD).

Abstract

Diffusion models have been applied to 3D LiDAR scene completion due to their strong training stability and high completion quality. However, the slow sampling speed limits the practical application of diffusion-based scene completion models since autonomous vehicles require an efficient perception of surrounding environments. This paper proposes a novel distillation method tailored for 3D LiDAR scene completion models, dubbed **ScoreLiDAR**, which achieves efficient yet high-quality scene completion. ScoreLiDAR enables the distilled model to sample in significantly fewer steps after distillation. To improve completion quality, we also introduce a novel **Structural Loss**, which encourages the distilled model to capture the geometric structure of the 3D LiDAR scene. The loss contains

a scene-wise term constraining the holistic structure and a point-wise term constraining the key landmark points and their relative configuration. Extensive experiments demonstrate that ScoreLiDAR significantly accelerates the completion time from 30.55 to 5.37 seconds per frame ($>5\times$) on SemanticKITTI and achieves superior performance compared to state-of-the-art 3D LiDAR scene completion models. Our model and code are publicly available on <https://github.com/happyw1nd/ScoreLiDAR>.

1. Introduction

Recognizing the surrounding environment accurately and efficiently using onboard sensors is crucial for the safe operation of autonomous vehicles [17, 18]. Among different types of sensors, 3D LiDAR has become one of the most

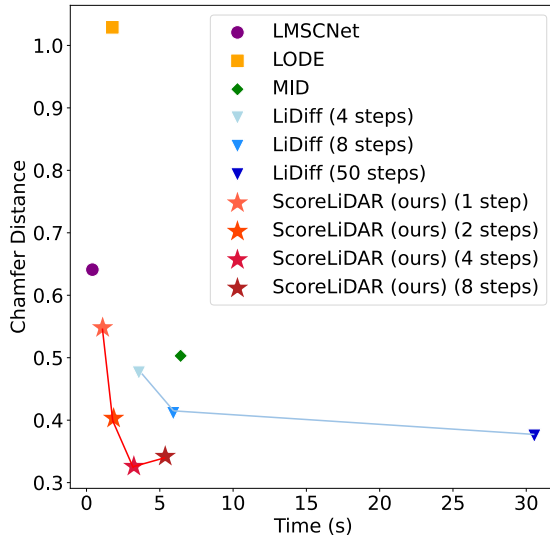


Figure 2. A visualization of LiDAR scene completion performances with different models on SemanticKITTI [1] dataset. Generally, our proposed ScoreLiDAR achieves better scene completion performance and speed trade-off.

widely adopted sensors due to its broader detection range and higher detection precision [25, 28]. However, driving scenarios are often complex, and the 3D point clouds collected by LiDAR are typically sparse, particularly in occluded areas [16, 38]. This sparsity causes a decline in the ability to understand 3D scenes [3, 28]. Thus, inferring and completing sparse 3D LiDAR scenes is necessary to provide a dense and more comprehensive scene representation.

Due to the advantages of strong training stability and high-generation quality, existing works utilize diffusion models to complete the 3D LiDAR scenes and achieve outstanding results [27, 28]. However, the diffusion model often requires multiple network iterations to obtain a dense, complete, and high-quality LiDAR scene, which is time-consuming [13, 54]. Autonomous vehicles require fast and efficient perception and recognition of surrounding environments, so the slow sampling speed limits the practical application of diffusion models. Although existing works have proposed acceleration methods for diffusion models [22, 33, 37, 40, 49], due to the differences between 3D LiDAR scenes and image data—where LiDAR scenes often contain complex geometric structure information—these techniques have not been explored in the acceleration of diffusion-based LiDAR scene completion model.

In this work, we propose **ScoreLiDAR**, a novel distillation method tailored for 3D LiDAR scene completion diffusion models, which enables efficient and high-quality scene completion (Fig. 1 and Fig. 2). ScoreLiDAR aims to tackle the unique 3D distribution alignment challenge in LiDAR scene completion. By exploiting a bidirectional gradient guidance mechanism, it allows the student model’s com-

pletion results under sparse point cloud conditions to progressively approach the multi-step iterative reconstruction quality of the teacher model. Given a completed scene generated by the student model, the teacher model predicts the scene’s score as a gradient to enhance realism, while a designed auxiliary model predicts the scene’s another score as a gradient to suppress unrealistic completion. The student model is then updated according to the difference between these two gradients. This update drives the completion process toward more structurally coherent LiDAR scenes. Finally, we introduce a **Structural Loss** consisting of a scene-wise term and a point-wise term constraining the key landmark points and their relative configuration. Prior studies [19, 23, 41, 42] demonstrated that the bidirectional gradient guidance mechanism can effectively accelerate 3D rendering speed. In this work, we argue that a similar approach can be directly applied to the distillation of diffusion-based LiDAR scene completion models.

Our contribution can be summarized as follows: (1) We propose **ScoreLiDAR**, a novel distillation method tailored for diffusion-based 3D LiDAR scene completion models, which achieves efficient scene completion. (2) We introduce a **Structural Loss** to effectively capture the geometric structure information of 3D point clouds during the distillation process, which ensures high-quality scene completion. (3) Extensive experiments show that ScoreLiDAR enables fast and efficient scene completion while achieving optimal generation quality compared to the existing models.

2. Related work

3D LiDAR Scene completion 3D LiDAR scene completion refers to recovering a complete scene from a sparse, incomplete LiDAR scan in applications such as autonomous driving [38, 46]. Current mainstream LiDAR scene completion methods include depth completion-based and Signed Distance Field (SDF)-based approaches. Depth completion-based methods aim to recover dense depth maps from sparse depth measurements [9, 43, 47]. These methods typically leverage deep learning techniques [4, 7] and can also incorporate guidance from RGB images to achieve higher-quality completion results [32, 50, 53]. SDF-based methods represent scenes as voxel grids, with the core idea of using signed distance fields to complete sparse LiDAR scenes [16, 38]. These methods are constrained by voxel resolution, making them prone to losing details within the scene [6, 28]. In addition, some methods introduce semantic information to enhance LiDAR scene completion [31, 44]. These methods can generate dense and complete scenes while providing semantic labels for each point, leading to broader application potential [39, 48].

Diffusion-based 3D LiDAR scene completion Due to the strong training stability and high generation quality of

diffusion models, many methods leverage diffusion models for LiDAR scene completion tasks [3, 14, 27–29]. The work of Lee *et al.* [14] is the first to apply diffusion models at the scene scale for LiDAR scene completion, enabling the generation of realistic scenes conditioned on partial observations from sparse point clouds. Similarly, R2DM [27] utilizes diffusion models based on distance and reflectance intensity image representations to generate various high-fidelity 3D LiDAR scenes. LiDiff [28] indicates that adding noise to point cloud data at the scene scale leads to a loss of detail. Therefore, LiDiff proposes operating directly on individual points and redefines the noise schedule and denoising processes to generate scenes with richer detail. Based on LiDiff, DiffSSC [3] further performs semantic scene completion tasks by implementing denoising and segmentation separately in both the point and semantic spaces. Moreover, LiDMs [29] constructs the pipeline from the perspectives of pattern realism, geometric realism, and object realism, achieving generation under different conditions.

Due to the slow sampling inherent in diffusion models, diffusion-based 3D LiDAR scene completion suffers from slow inference, hindering its application in autonomous vehicles. Thus, this paper proposes a distillation method for diffusion-based 3D LiDAR scene completion models to achieve faster and higher-quality completion.

3. Preliminary

3.1. Brief introduction of diffusion models

The diffusion models have two processes: forward diffusion and reverse denoising process [10, 34]. In the forward diffusion process, given the data $\mathbf{x}^0 \sim q(\mathbf{x})$ from the training distribution, the diffusion model adds different scales of noise to \mathbf{x}^0 according to different timesteps $t \in [1, T]$ to obtain noisy data $\{\mathbf{x}^1, \mathbf{x}^2, \dots, \mathbf{x}^T\}$. When T is large enough, \mathbf{x}^T approaches to standard Gaussian distribution, namely, $q(\mathbf{x}^T) \approx \mathcal{N}(0, I)$. This process is parameterized by a series of predefined noise factors β^t . By defining $\alpha^t = 1 - \beta^t$, the diffusion process is expressed as [10]:

$$\mathbf{x}^t = \sqrt{\bar{\alpha}^t} \mathbf{x}^0 + \sqrt{1 - \bar{\alpha}^t} \boldsymbol{\epsilon}^t \quad (1)$$

Here $\bar{\alpha}^t = \prod_{i=1}^t \alpha^i$, $p(\mathbf{x}^t | \mathbf{x}^0) = \mathcal{N}(\sqrt{\bar{\alpha}^t}, (1 - \bar{\alpha}^t)I)$.

During the training, the diffusion model tries to predict the added noise at different timesteps t . Given the input \mathbf{x}^0 and the condition c (optional), the noisy data \mathbf{x}^t can be calculated by Eq. (1). The diffusion model ϵ_θ predicts the noise according to \mathbf{x}^t, c, t and is then optimized by calculating the ℓ_2 loss between the predicted and the real noise.

$$\mathcal{L}_{DM} = \mathbb{E}_{t, \epsilon} [\|\boldsymbol{\epsilon} - \epsilon_\theta(\mathbf{x}^t, c, t)\|^2] \quad (2)$$

Here θ is the trainable parameter of ϵ_θ .

In the reverse denoising process, the diffusion model starts from the timestep T and progressively removes the

predicted noise to obtain a generated sample. The process of denoising \mathbf{x}^t to obtain \mathbf{x}^{t-1} can be written as in [10]

$$\mathbf{x}^{t-1} = \frac{1}{\sqrt{\alpha^t}} \left(\mathbf{x}^t - \frac{1 - \alpha^t}{\sqrt{1 - \bar{\alpha}^t}} \epsilon_\theta(\mathbf{x}^t, c, t) \right) + \sigma^t \mathbf{z} \quad (3)$$

Here $\mathbf{z} \sim \mathcal{N}(0, I)$. In this process, the number of required inference steps varies depending on different sampling methods. For instance, DDPM [10] requires 1000 timesteps, while DDIM [34] and DPM solver [21] can reduce this to no more than 100 timesteps.

3.2. 3D LiDAR scene completion diffusion models

The 3D LiDAR scene completion diffusion models take the incomplete scan $\mathcal{P} = \{\mathbf{p}_1, \mathbf{p}_2, \dots, \mathbf{p}_N\}$ ($\mathbf{p}_i \in \mathbb{R}^3$) and try to generate the complete scene $\mathcal{G}^0 = \{\mathbf{p}_1^0, \mathbf{p}_2^0, \dots, \mathbf{p}_M^0\}$. Given the input LiDAR scan \mathcal{P} and ground truth \mathcal{G} , a diffusion model can be trained to perform 3D LiDAR scene completion. The noisy scene \mathcal{G}^t at timestep t is calculated from the ground truth \mathcal{G} at point level [3, 28],

$$\mathbf{p}_m^t = \sqrt{\bar{\alpha}^t} \mathbf{p}_m + \sqrt{1 - \bar{\alpha}^t} \boldsymbol{\epsilon}^t, \forall \mathbf{p}_m \in \mathcal{G} \quad (4)$$

Here $\mathcal{G}^t = \{\mathbf{p}_1^t, \mathbf{p}_2^t, \dots, \mathbf{p}_M^t\}$. Because the LiDAR point cloud is sparse, the noisy data retains very little information about the original data. To generate more realistic point cloud scenes, the LiDAR scan \mathcal{P} can be used as a condition of the diffusion model [28]. In this case, the training loss of the diffusion model is given by:

$$\mathcal{L}_{DM} = \mathbb{E}_{t, \epsilon} [\|\boldsymbol{\epsilon} - \epsilon_\theta(\mathcal{G}^t, \mathcal{P}, t)\|^2] \quad (5)$$

Then, as described in Sec. 3.1, the completed scene \mathcal{G}^0 can be generated by progressive denoising from \mathcal{G}^T . Because the scale of the LiDAR scene is large and the data range is different across different point cloud axes, directly normalizing the entire scene compresses the data into a smaller range, which potentially leads to the loss of critical details [3, 28]. To solve this issue, LiDiff [28] modifies the diffusion process by adding a local noise offset to each point \mathbf{p}_m , gradually perturbing the point cloud at each timestep. For Eq. (1), \mathbf{x}^0 is set to 0, and \mathbf{x}^t is added to each point \mathbf{p}_m ,

$$\mathbf{p}_m^t = \mathbf{p}_m + \left(\sqrt{\bar{\alpha}^t} \mathbf{0} + \sqrt{1 - \bar{\alpha}^t} \boldsymbol{\epsilon}^t \right) = \mathbf{p}_m + \sqrt{1 - \bar{\alpha}^t} \boldsymbol{\epsilon}^t \quad (6)$$

Due to this special case, the initial noisy scene \mathcal{G}^T cannot directly start from standard Gaussian noise in the sampling process. Instead, the LiDAR scan \mathcal{P} is used to obtain \mathcal{G}^T [28]. Firstly, given the initial incomplete scan \mathcal{P} , the number of the point clouds is increased by duplicating the original points K times and getting the pseudo dense scan $\mathcal{P}^* = \{\mathbf{p}_1^*, \mathbf{p}_2^*, \dots, \mathbf{p}_M^*\}$, where we assume $M = KN$. Then, we calculate the noisy point cloud \mathcal{P}^T by Eq. (6). As \mathcal{P}^T is noisy enough, it can be regarded as \mathcal{G}^T during the training. After that, a step-by-step denoising process is applied to obtain the completed scene \mathcal{G}^0 .

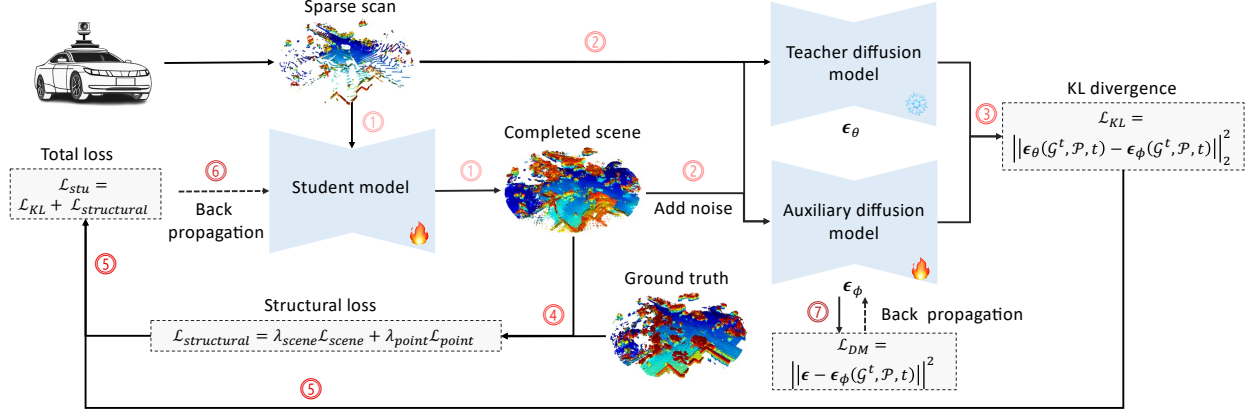


Figure 3. The overall structure of ScoreLiDAR. (1) The student model generates the completed scene based on the sparse scan. (2) The sparse scan and noisy completed scene are input to ϵ_θ and ϵ_ϕ . (3) The predicted score of ϵ_θ and ϵ_ϕ are used to calculate the KL divergence. (4) Structural loss is calculated based on the completed scene and the ground truth. (5) The total loss is calculated with KL divergence and structural loss. (6) The student model is optimized according to the total loss. (7) The diffusion model ϵ_ϕ is updated with the completed scene.

4. Method

Our goal is to distill a pre-trained 3D LiDAR scene completion diffusion model into a student model with significantly fewer sampling steps, enabling efficient and high-quality scene completion. Firstly, we introduce the distillation method tailored for 3D LiDAR scene completion diffusion models in Sec. 4.1. Then, we introduce the structural loss to improve the distillation process with both scene-wise loss and point-wise loss in Sec. 4.2. Finally, we describe the optimization procedure of ScoreLiDAR in Sec. 4.3. The overall structure of ScoreLiDAR is shown in Fig. 3.

4.1. Distillation for 3D LiDAR scene completion

Ideally, the final student model would achieve completion results comparable to those of the teacher model at a faster speed. In the 3D LiDAR scene completion scenario, let q be the distribution of the ground truth \mathcal{G} , and ϵ_θ be the pre-trained scene completion diffusion model whose multi-step generated distribution approximates q^0 . Let G_{stu} be the student model that can perform efficient LiDAR scene completion with the generated distribution p_G^0 . ScoreLiDAR aims to minimize the KL divergence between the distribution of the teacher model and the generated distribution of the student model [42, 52].

$$\min_{\eta} D_{KL}(p_G^0(\mathcal{G}^0; \eta) \| q^0(\mathcal{G}^0)) \quad (7)$$

Here \mathcal{G}^0 is the completed scene generated by one-step sampling of G_{stu} conditioned on \mathcal{P} , for simplicity, we omit \mathcal{P} when representing the distribution, η is the trainable parameter of G_{stu} . However, the high-density regions of q^0 are sparse in the data space, so it is hard to directly solve Eq. (7). According to Theorem 1 in [42], we expand the optimization problems in Eq. (7) by minimizing the KL divergence

between two distributions at different noise levels as:

$$\min_{\eta} \mathcal{L}_{KL} = \mathbb{E}_{t, \epsilon} [D_{KL}(p_G^t(\mathcal{G}^t) \| q^t(\mathcal{G}^t))] \quad (8)$$

Here t is the timestep controlling the noise level, ϵ is random noise, and $\mathcal{G}^t = \{p_1^t, p_2^t, \dots, p_M^t\}$ is the noisy version of the completed scene \mathcal{G}^0 at timestep t . The gradient of G_{stu} in Eq. (8) is approximated by

$$\begin{aligned} & \nabla_{\eta} D_{KL}(p_G^t(\mathcal{G}^t) \| q^t(\mathcal{G}^t)) \\ &= \mathbb{E}_{t, \epsilon} [\nabla_{\mathcal{G}^t} \log p_G^t(\mathcal{G}^t) - \nabla_{\mathcal{G}^t} \log q^t(\mathcal{G}^t)] \frac{\partial \mathcal{G}^t}{\partial \eta} \end{aligned} \quad (9)$$

We use the pre-trained diffusion model ϵ_θ to approximate $-\sqrt{1 - \bar{\alpha}^t} \nabla_{\mathcal{G}^t} \log q^t(\mathcal{G}^t)$ as discussed in Section 5 of Supplementary Materials (Sec S5). Similarly, $-\sqrt{1 - \bar{\alpha}^t} \nabla_{\mathcal{G}^t} \log p_G^t(\mathcal{G}^t)$ is approximated by an auxiliary diffusion model ϵ_ϕ , which is independently trained with the denoising loss Eq. (5) on generated samples \mathcal{G}^0 . Then, with the simplification as in [10, 42], the \mathcal{L}_{KL} is estimated by

$$\mathcal{L}_{KL} \approx \mathbb{E}_{t, \epsilon} [\|\epsilon_\theta(\mathcal{G}^t, \mathcal{P}, t) - \epsilon_\phi(\mathcal{G}^t, \mathcal{P}, t)\|_2^2] \quad (10)$$

Thus, the gradient in Eq. (9) is approximated by

$$\begin{aligned} & \nabla_{\eta} D_{KL}(p_G^t(\mathcal{G}^t) \| q^t(\mathcal{G}^t)) \\ & \approx \mathbb{E}_{t, \epsilon} [\epsilon_\theta(\mathcal{G}^t, \mathcal{P}, t) - \epsilon_\phi(\mathcal{G}^t, \mathcal{P}, t)] \frac{\partial \mathcal{G}^t}{\partial \eta} \end{aligned} \quad (11)$$

Intuitively, the orientation of $-\epsilon_\theta(\mathcal{G}^t, \mathcal{P}, t)$ points to the pre-trained distribution, while that of $-\epsilon_\phi(\mathcal{G}^t, \mathcal{P}, t)$ points to the student model's generative distribution. Thus, decenting along the bidirectional gradient $[\epsilon_\theta(\mathcal{G}^t, \mathcal{P}, t) - \epsilon_\phi(\mathcal{G}^t, \mathcal{P}, t)]$ updates the student model's generative distribution toward the pre-trained distribution, achieving a more accurate completion. Sec S2.1 discusses the efficiency of the distillation process.

4.2. Structural loss

Although the distillation process in Sec. 4.1 is effective in training models [22, 54], we found that directly applying it to LiDAR scene completion diffusion models leads to loss of local details and reduced realism. This is because the point cloud in LiDAR scenes includes complex geometric information that is not explicitly captured by diffusion models. Thus, we introduce a structural loss to further refine the distillation process and improve the completion quality. This structural loss includes scene-wise loss and point-wise loss and can help the student model effectively capture geometric structure information of the 3D point clouds.

Scene-wise loss. In the distillation process mentioned in Sec. 4.1, the gradient $\nabla_\eta D_{KL}$ in Eq. (11) is well-defined when $t \gg 0$, *i.e.* the generated samples are totally disturbed by Gaussian noise. However, $\nabla_\eta D_{KL}$ becomes unreliable when t is small [52, 54]. This is because the student model often generates subpar results at the early stage due to the complexity of the point cloud data. It is easy for the noisy generated samples to lie outside the training distribution of the teacher model, causing the unreliable network prediction of the teacher model [52, 54].

To solve this issue, we introduce the scene-wise loss, which minimizes the distance between the ground truth scene \mathcal{G} and the completed scene \mathcal{G}^0 ,

$$\mathcal{L}_{scene} = \frac{1}{|\mathcal{G}^0|} \sum_{\mathbf{p}_i^0 \in \mathcal{G}^0} \min_{\mathbf{p} \in \mathcal{G}} \|\mathbf{p}_i^0 - \mathbf{p}\|^2 \quad (12)$$

This loss calculates the mean squared error between each point \mathbf{p}_i^0 in the generated scene \mathcal{G}^0 and its closest corresponding point \mathbf{p} in the ground truth \mathcal{G} . It helps the student model capture the holistic structure, which prevents the optimization direction from deviating in the early stages and enhances training stability. The scene-wise loss enables the generated scenes to be closer to the ground truth globally, thereby enhancing the completion quality and fidelity.

Point-wise loss. As seen in Eq. (11), the distillation process only constrains the overall distribution of the completed scene, ignoring the relative positions between different points. Directly using the gradient in Eq. (11) to optimize the student model may lead to loss of local details.

Thus, we introduce the point-wise loss to capture the relative structural information between different points in the 3D LiDAR scene. The point-wise loss calculates the difference between the inter-point distance matrices of the completed scene and the ground truth. Due to the large number of points in the scene, calculating the distance matrix for all points is computationally intensive. Therefore, we select n key points to compute the distance matrix with $n \ll M$. Based on the local geometric features of each point, we

choose key points that are critical for representing the structure of the 3D LiDAR scene. For each point \mathbf{p}_i^0 in the completed scene \mathcal{G}^0 , we find its K-nearest neighbor, denoted as the set \mathcal{K}_i . Then we select the key points by calculating their curvature κ_i . The specific steps are as follows:

- Calculate the centroid $\bar{\mathbf{p}}_i^0$ of the neighborhood \mathcal{K}_i

$$\bar{\mathbf{p}}_i^0 = \frac{1}{K} \sum_{\mathbf{p}_j^0 \in \mathcal{K}_i} \mathbf{p}_j^0 \quad (13)$$

- Calculate the neighborhood covariance matrix \mathcal{C}_i for $\bar{\mathbf{p}}_i^0$

$$\mathcal{C}_i = \frac{1}{K} \sum_{\mathbf{p}_j^0 \in \mathcal{K}_i} (\mathbf{p}_j^0 - \bar{\mathbf{p}}_i^0)(\mathbf{p}_j^0 - \bar{\mathbf{p}}_i^0)^T \quad (14)$$

- Perform eigen-decomposition on the covariance matrix \mathcal{C}_i to obtain the eigenvalues $\lambda_1 < \lambda_2 < \dots < \lambda_m$.
- Curvature κ_i can be calculated using the eigenvalues

$$\kappa_i = \frac{\lambda_1}{\sum_{j=1}^m \lambda_j} \quad (15)$$

A larger curvature κ_i indicates greater local shape variation. Those points with great local variation are typically located at corners, edges, or endpoints, which tend to shape the main structure of the scene. Therefore, the top n points with the highest curvature values are selected as key points.

Given the ground truth $\mathcal{G} = \{\mathbf{p}_1, \mathbf{p}_2, \dots, \mathbf{p}_M\}$, we select n key points ($n \ll M$) from the point cloud to construct the $n \times n$ distance matrix \mathcal{D} . The $d_{ij} \in \mathcal{D}$ represents the pairwise Euclidean Distance between points i and j . Then, for completed scene \mathcal{G}^0 , we select n points that are closest to the key points in \mathcal{G} as the corresponding key points to obtain the distance matrix \mathcal{D}_G . Thus, the point-wise loss is calculated by

$$\mathcal{L}_{point} = \mathbb{E}_{t,\epsilon} [\|\mathcal{D} - \mathcal{D}_G\|_2^2] \quad (16)$$

The point-wise loss can help the student model capture the relative configuration of key points and further enhance the geometric accuracy and detail retention of the completed scene. This ensures that key objects like cars, traffic cones, and walls are better completed, which is crucial for autonomous vehicles to recognize surroundings accurately.

Structural loss. The final structural loss of G_{stu} is

$$\mathcal{L}_{structural} = \lambda_{scene} \mathcal{L}_{scene} + \lambda_{point} \mathcal{L}_{point} \quad (17)$$

Here λ_{scene} and λ_{point} are the weight of scene-wise loss and point-wise loss.

Model	CD ↓	JSD ↓	EMD ↓	Times (s) ↓
LMSCNet [30]	0.641	0.431	-	0.40
LODE [16]	1.029	0.451	-	1.76
MID [38]	0.503	0.470	-	6.42
PVD [55]	1.256	0.498	-	262.54
LiDiff [28]	0.434	0.444	22.15	30.38
LiDiff (Refined) [28]	0.375	0.416	23.16	30.55
ScoreLiDAR	0.406	0.425	23.14	5.16
ScoreLiDAR (Refined)	0.342	0.399	23.26	5.37

Table 1. The completion performance on the SemanticKITTI dataset. Colors denote the 1st, 2nd, and 3rd best-performing model. The sampling time is estimated based on the official code and the provided checkpoints.

Model	CD ↓	JSD ↓	EMD ↓	Times (s) ↓
LMSCNet [30]	0.979	0.496	-	0.38
LODE [16]	1.565	0.483	-	1.64
MID [38]	0.637	0.476	-	6.23
LiDiff [28]	0.564	0.459	21.98	29.18
LiDiff (Refined) [28]	0.517	0.446	22.96	29.43
ScoreLiDAR	0.472	0.444	22.80	4.98
ScoreLiDAR (Refined)	0.452	0.437	23.02	5.14

Table 2. The completion performance on the KITTI-360 dataset. The meaning of notations is the same as those in Tab. 1.

Model	SemanticKITTI			KITTI360		
	CD ↓	JSD ↓	EMD ↓	CD ↓	JSD ↓	EMD ↓
ScoreLiDAR (Refined)	0.342	0.399	23.26	0.452	0.437	23.02
w/o Structural Loss (Refined)	0.419	0.430	24.61	0.549	0.445	24.56

Table 3. Ablation study of the structural loss.

4.3. Optimization procedure

During the training, G_{stu} and ϵ_ϕ are initialized with the teacher model ϵ_θ and optimized alternately. The auxiliary diffusion model ϵ_ϕ is trained on the completed scene of the student model with Eq. (5). As for G_{stu} , we follow the proposed method to select $\frac{1}{30}$ of the points from the entire point cloud as key points for calculating the point distance matrix. Then, G_{stu} is optimized with the following objective

$$\mathcal{L}_{stu} = \mathcal{L}_{KL} + \mathcal{L}_{structural} \quad (18)$$

We set $\lambda_{scene} = 0.5$ and $\lambda_{point} = 0.01$ defaultly. The implementation details are provided in Sec S1.

5. Experiment

In this part, we conduct a series of experiments to evaluate the effectiveness of the proposed ScoreLiDAR. We compare ScoreLiDAR with advanced models including LMSCNet [30], LODE [16], MID [38], PVD [55] and LiDiff [28]. We first evaluate the performance of ScoreLiDAR in scene

Model	CD ↓	JSD ↓	EMD ↓	Time (s) ↓
LiDiff (50 steps) [28]	0.434	0.444	22.15	30.38
LiDiff (50 steps Refined) [28]	0.375	0.416	23.16	30.55
LiDiff (8 steps) [28]	0.447	0.432	24.90	5.69
LiDiff (8 steps Refined) [28]	0.411	0.406	25.74	5.92
ScoreLiDAR (8 Steps Refined)	0.342	0.399	23.14	5.37
ScoreLiDAR (4 Steps Refined)	0.326	0.386	23.98	3.23
ScoreLiDAR (2 Steps Refined)	0.403	0.379	-	1.85
ScoreLiDAR (1 Steps Refined)	0.548	0.384	-	1.10

Table 4. Ablation study of different sampling steps on the SemanticKITTI dataset.

completion tasks (Sec. 5.1). Secondly, we present the results of ablation studies showing the effectiveness of the structural loss and the performances of ScoreLiDAR given different sampling steps (Sec. 5.2). Finally, we further evaluate ScoreLiDAR with the qualitative analysis (Sec. 5.3).

5.1. Scene completion

We validate ScoreLiDAR on SemanticKITTI [1] and KITTI-360 [20] datasets. The existing SOTA LiDAR scene completion model LiDiff [28] is chosen as the teacher model. The student model shares the network architecture with the teacher model and is initialized by the teacher model. Moreover, we also use the refinement network in LiDiff [28] to refine the completed scene generated by the student model. We calculate the Chamfer Distance (CD) [2], the Jensen-Shannon Divergence (JSD) [24] and the Earth Mover’s Distance (EMD) [8] to evaluate the similarity between the completed scene and the ground truth. The smaller the value of these metrics, the closer the completed scene is to the ground truth.

Tab. 1 shows that ScoreLiDAR achieves the optimal performance compared to the existing models in most cases on the SemanticKITTI dataset. Compared to the SOTA method LiDiff [28] with refinement, which takes 30.55 seconds to complete a scene, ScoreLiDAR completes a scene in just 5.47 seconds (fivefold speedup) yet with 8% improvement in CD, 4% in JSD, and comparable results in EMD. The reason for the increase in EMD after refinement is the mismatch in the points numbers between \mathcal{G}^0 and \mathcal{G} , leading to a higher matching cost. The refinement process optimizes local details but alters the global point cloud distribution, extending the overall transfer path. Although LMSCNet [30] and LODE [16] have faster completion speeds, their completion quality is significantly lower. The performance of ScoreLiDAR outperforms the teacher model LiDiff [28]. This is because ScoreLiDAR introduces a structural loss with scene-wise term and point-wise term, enabling the student model to effectively capture geometric structure information within LiDAR point cloud data during training. Results on KITTI-360 are shown in Tab. 2. ScoreLiDAR also achieves optimal performance in most cases and boasts

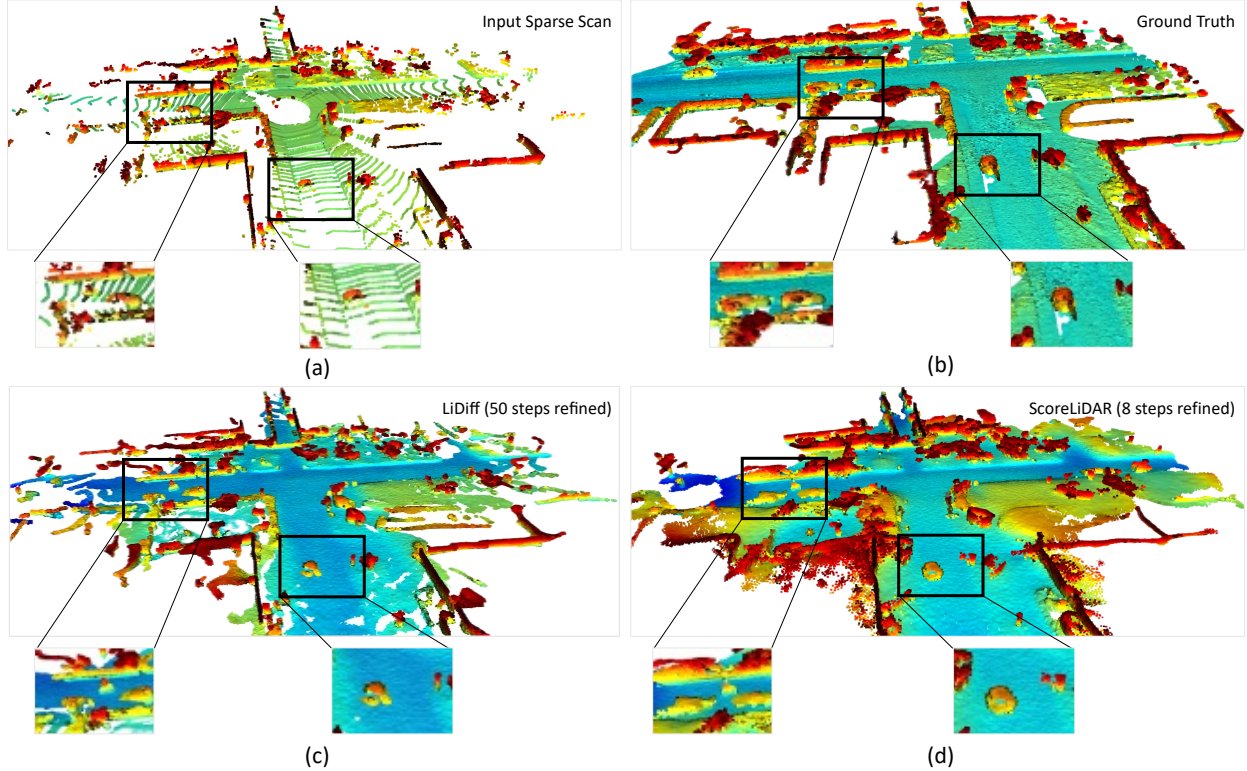


Figure 4. Qualitative results on KITTI-360. ScoreLiDAR achieves better completion than LiDiff [29] with fewer sampling steps.

a fivefold speedup with 12% improvement in CD and 2% in JSD compared to LiDiff [28].

5.2. Ablation study

In this part, we conduct the ablation study to verify the effectiveness of the structural loss in the training of the proposed ScoreLiDAR. We compared the scene completion performances of the proposed ScoreLiDAR with a variant that does not incorporate structural loss. The results are shown in Tab. 3. The results show that the variant without structural loss exhibits lower performance in scene completion on both datasets. However, after considering the structural loss, the performance of ScoreLiDAR improves significantly, which achieves better performance on all metrics. This supports our discussion in Sec. 4.3, incorporating structural loss enables the student model to capture the geometric structure feature of 3D point clouds, thereby facilitating the effective distillation of the student model.

Furthermore, we compared the scene completion performance of ScoreLiDAR with different sampling steps, and the results are shown in Tab. 4. It can be observed that as the sampling steps decrease from 8 to 1, the time required for ScoreLiDAR to complete a scene also decreases, with single-step sampling allowing a scene to be completed in only 1.1 seconds. With 8-step and 4-step sampling, ScoreLiDAR performs better than LiDiff. All metrics decay

2-step and 1-step sampling, but in JSD ours still performs better than LiDiff. In summary, although the quality of scene completion decreases as the sampling steps are reduced, it still maintains performance comparable to or better than the existing model, achieving better performance and speed trade-off as in Fig. 2.

In addition, we compared the ablation results about the terms of structural loss, different keypoint selection methods, varying numbers of keypoints, and different values of λ_{scene} and λ_{point} and so on, which are presented in Sec. S4.

5.3. Qualitative analysis

Fig. 4 shows the completed scenes by our proposed ScoreLiDAR and LiDiff [28] on KITTI-360. ScoreLiDAR achieves completion results with higher quality and greater fidelity in less time compared to LiDiff. For example, as shown in Fig. 4(c), in the left region, there should be two vehicles as in Fig. 4(b), but the scene completed by LiDiff only contains one. In contrast, the scene completed by ScoreLiDAR with only 8 steps in Fig. 4(d) completes two vehicles and has clearer and more complete vehicle structures, making it closer to the ground truth.

To further demonstrate the effectiveness of ScoreLiDAR and the structural loss, we calculate the distance between the points in the completed scene and their corresponding points in the ground truth to evaluate the overall differ-

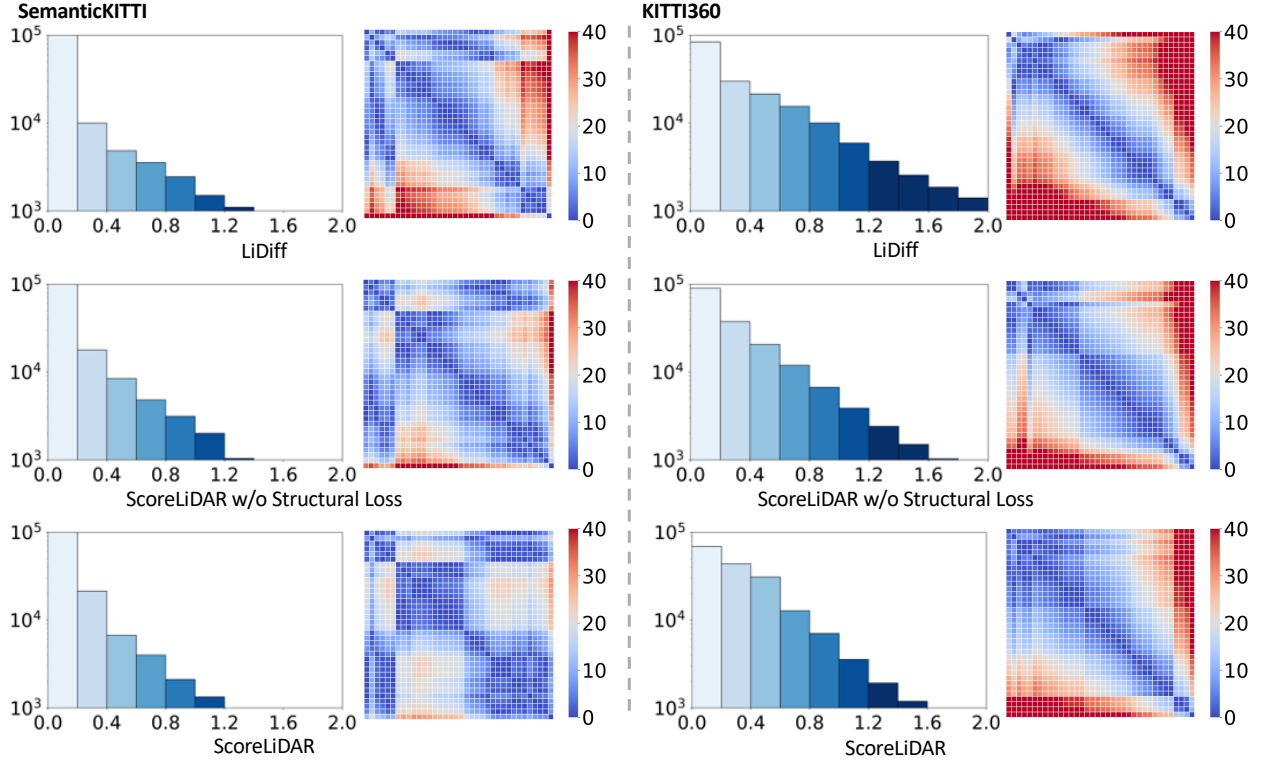


Figure 5. The qualitative analysis of structural loss. The bar chart shows the distribution of distances between corresponding points in the completed and ground truth scenes. A higher number of points with smaller distances demonstrates that the completed scene is closer to the ground truth. The heatmap represents the difference in distance matrices between the completed scene and the ground truth scene. Smaller values on the heatmap indicate that the completed scene is closer to the ground truth.

ence. We display the calculated results in bar chart in Fig. 5. ScoreLiDAR has the highest number of points with smaller distances to their corresponding points in the ground truth. The results show that the scenes completed by ScoreLiDAR are closer to the ground truth overall, demonstrating higher fidelity. Moreover, we selected 36 corresponding key points from the ground truth and the completed scene using the method described in Sec. 4.2 and calculated the point distance matrices \mathcal{D} and \mathcal{D}_G . We then visualized the difference between \mathcal{D} and \mathcal{D}_G as a heatmap. As shown in Fig. 5, on both datasets, the difference of point distance matrix between the completed scene of LiDiff [28] and the ground truth is the largest, followed by the ScoreLiDAR variant without the structural loss and the smallest difference is achieved by ScoreLiDAR. This also indicates that the scene completed by ScoreLiDAR is closer to the ground truth.

We also conduct a user study to evaluate the performance of ScoreLiDAR. We used ScoreLiDAR and LiDiff [28] to complete scenes based on the same input scans and asked users to choose the scene they believed was closer to the ground truth. ScoreLiDAR received a 65% user preference over LiDiff [28]. This indicates that the detail and fidelity of the scenes completed by ScoreLiDAR more closely resemble the ground truth for most users. The details of the

user study are shown in SM.

6. Conclusion

Summary. This paper proposes ScoreLiDAR, a novel distillation method tailored for 3D LiDAR scene completion diffusion models based on a bidirectional gradient guidance mechanism. By introducing the structural loss with scene-wise term and point-wise term, ScoreLiDAR trains the student model to effectively capture the holistic structure and the relative configuration of key points and achieve efficient and high-quality scene completion.

Limitations. While ScoreLiDAR achieves efficient, high-quality LiDAR scene completion, its performance is constrained by the teacher model. As the performance of the teacher model improves, so does the capability of the student model. Although we conducted a preliminary experiment on the semantic scene completion in the Supplementary Material, a more comprehensive exploration is still required. Thus, further exploration is required to find a more effective method to improve the training process of ScoreLiDAR and avoid the limitations of the teacher model, achieving more efficient semantic LiDAR scene completion.

Acknowledgement

This paper is supported by Provincial Key Research and Development Plan of Zhejiang Province under No. 2024C01250(SD2), National Natural Science Foundation of China (Grant No. 62006208) and Dream Set Off - Kunpeng & Ascend Seed Program.

References

- [1] Jens Behley, Martin Garbade, Andres Milioto, Jan Quenzel, Sven Behnke, Cyrill Stachniss, and Jürgen Gall. Semantickitti: A Dataset For Semantic Scene Understanding Of Lidar Sequences. In *ICCV*, pages 9297–9307, 2019. [1](#), [2](#), [11](#)
- [2] M Akmal Butt and Petros Maragos. Optimum Design of Chamfer Distance Transforms. *TIP*, 7(10):1477–1484, 1998. [6](#), [11](#)
- [3] Helin Cao and Sven Behnke. DiffSSC: Semantic LiDAR Scan Completion Using Denoising Diffusion Probabilistic Models. *arXiv preprint arXiv:2409.18092*, 2024. [2](#), [3](#)
- [4] Nathaniel Chodosh, Chaoyang Wang, and Simon Lucey. Deep Convolutional Compressed Sensing For Lidar Depth Completion. In *ACCV*, pages 499–513, 2019. [2](#)
- [5] Christopher Choy, JunYoung Gwak, and Silvio Savarese. 4D Spatio-Temporal ConvNets: Minkowski Convolutional Neural Networks. In *CCPR*, pages 3075–3084, 2019. [17](#)
- [6] Angela Dai, Daniel Ritchie, Martin Bokeloh, Scott Reed, Jürgen Sturm, and Matthias Nießner. Scancomplete: Large-Scale Scene Completion And Semantic Segmentation For 3d Scans. In *CVPR*, pages 4578–4587, 2018. [2](#)
- [7] Abdelrahman Eldekokey, Michael Felsberg, and Fahad Shahbaz Khan. Confidence Propagation Through CNNs For Guided Sparse Depth Regression. *PAMI*, 42(10):2423–2436, 2019. [2](#)
- [8] Haoqiang Fan, Hao Su, and Leonidas J Guibas. A Point Set Generation Network for 3d Object Reconstruction From a Single Image. In *CVPR*, pages 605–613, 2017. [6](#)
- [9] Chen Fu, Christoph Mertz, and John M Dolan. Lidar and Monocular Camera Fusion: On-road Depth Completion For Autonomous Driving. In *ITCS*, pages 273–278, 2019. [2](#)
- [10] Jonathan Ho, Ajay Jain, and Pieter Abbeel. Denoising Diffusion Probabilistic Models. *NIPS*, 33:6840–6851, 2020. [3](#), [4](#), [12](#), [13](#)
- [11] Edward J Hu, Phillip Wallis, Zeyuan Allen-Zhu, Yuanzhi Li, Shean Wang, Lu Wang, Weizhu Chen, et al. LoRA: Low-Rank Adaptation Of Large Language Models. In *ICLR*, 2021. [17](#)
- [12] Jaehoon Jung, Michael J Olsen, David S Hurwitz, Alireza G Kashani, and Kamilah Buker. 3D Virtual Intersection Sight Distance Analysis Using LiDAR Data. *Transportation research part C: emerging technologies*, 86:563–579, 2018. [13](#)
- [13] Dongjun Kim, Chieh-Hsin Lai, Wei-Hsiang Liao, Naoki Murata, Yuhta Takida, Toshimitsu Uesaka, Yutong He, Yuki Mitsufuji, and Stefano Ermon. Consistency Trajectory Models: Learning Probability Flow ODE Trajectory of Diffusion. In *ICLR*, 2024. [2](#)
- [14] Jumin Lee, Woobin Im, Sebin Lee, and Sung-Eui Yoon. Diffusion Probabilistic Models For Scene-Scale 3d Categorical Data. *arXiv preprint arXiv:2301.00527*, 2023. [3](#), [13](#)
- [15] Jumin Lee, Sebin Lee, Changho Jo, Woobin Im, Juhyeong Seon, and Sung-Eui Yoon. Semicity: Semantic Scene Generation With Triplane Diffusion. In *CVPR*, pages 28337–28347, 2024. [15](#)
- [16] Pengfei Li, Ruowen Zhao, Yongliang Shi, Hao Zhao, Jirui Yuan, Guyue Zhou, and Ya-Qin Zhang. Lode: Locally Conditioned Eikonal Implicit Scene Completion From Sparse Lidar. In *ICRA*, pages 8269–8276, 2023. [2](#), [6](#), [13](#), [15](#)
- [17] You Li, Julien Moreau, and Javier Ibanez-Guzman. Emergent Visual Sensors For Autonomous Vehicles. *IEEE Transactions on Intelligent Transportation Systems*, 24(5):4716–4737, 2023. [1](#), [13](#)
- [18] Yiming Li, Zhiding Yu, Christopher Choy, Chaowei Xiao, Jose M Alvarez, Sanja Fidler, Chen Feng, and Anima Anandkumar. Voxformer: Sparse Voxel Transformer For Camera-based 3d Semantic Scene Completion. In *CVPR*, pages 9087–9098, 2023. [1](#), [13](#)
- [19] Yixun Liang, Xin Yang, Jiantao Lin, Haodong Li, Xiaogang Xu, and Yingcong Chen. Luciddreamer: Towards High-fidelity Text-to-3d Generation Via Interval Score Matching. In *CVPR*, pages 6517–6526, 2024. [2](#)
- [20] Yiyi Liao, Jun Xie, and Andreas Geiger. Kitti-360: A Novel Dataset And Benchmarks For Urban Scene understanding in 2d And 3d. *PAMI*, 45(3):3292–3310, 2022. [1](#), [6](#), [11](#)
- [21] Cheng Lu, Yuhao Zhou, Fan Bao, Jianfei Chen, Chongxuan Li, and Jun Zhu. Dpm-solver: A Fast Ode Solver For Diffusion Probabilistic Model Sampling In Around 10 Steps. *NIPS*, 35:5775–5787, 2022. [3](#)
- [22] Weijian Luo, Tianyang Hu, Shifeng Zhang, Jiacheng Sun, Zhenguo Li, and Zhihua Zhang. Diff-Instruct: A Universal Approach for Transferring Knowledge From Pre-trained Diffusion Models. *NIPS*, 36:76525–76546, 2023. [2](#), [5](#), [12](#)
- [23] Zhiyuan Ma, Yuxiang Wei, Yabin Zhang, Xiangyu Zhu, Zhen Lei, and Lei Zhang. Scaledreamer: Scalable Text-to-3d Synthesis With Asynchronous Score Distillation. In *ECCV*, pages 1–19, 2024. [2](#)
- [24] María Luisa Menéndez, JA Pardo, L Pardo, and MC Pardo. The Jensen-Shannon Divergence. *Journal of the Franklin Institute*, 334(2):307–318, 1997. [6](#), [11](#)
- [25] Amir Meydani. State-of-the-Art Analysis Of The Performance Of The Sensors Utilized In Autonomous Vehicles In Extreme Conditions. In *Proceedings of the International Conference on Artificial Intelligence and Smart Vehicles*, pages 137–166, 2023. [2](#)
- [26] Ben Mildenhall, Pratul P Srinivasan, Matthew Tancik, Jonathan T Barron, Ravi Ramamoorthi, and Ren Ng. Nerf: Representing scenes as neural radiance fields for view synthesis. *Communications of the ACM*, 65(1):99–106, 2021. [16](#)
- [27] Kazuto Nakashima and Ryo Kurazume. Lidar Data Synthesis With Denoising Diffusion Probabilistic Models. In *ICRA*, pages 14724–14731, 2024. [2](#), [3](#)
- [28] Lucas Nunes, Rodrigo Marcuzzi, Benedikt Mersch, Jens Behley, and Cyrill Stachniss. Scaling Diffusion Models To

Real-World 3D LiDAR Scene Completion. In *CVPR*, pages 14770–14780, 2024. 1, 2, 3, 6, 7, 8, 11, 12, 13, 14, 15

[29] Haoxi Ran, Vitor Guizilini, and Yue Wang. Towards Realistic Scene Generation With LiDAR Diffusion Models. In *CVPR*, pages 14738–14748, 2024. 3, 7, 13

[30] Luis Roldao, Raoul de Charette, and Anne Verroust-Blondet. Lmscnet: Lightweight Multiscale 3d Semantic Completion. In *Proceedings of International Conference on 3D Vision*, pages 111–119, 2020. 6, 15

[31] Luis Roldao, Raoul De Charette, and Anne Verroust-Blondet. 3D Semantic Scene Completion: A Survey. *International Journal of Computer Vision*, 130(8):1978–2005, 2022. 2

[32] Kwonyoung Ryu, Kang-il Lee, Jegyeong Cho, and Kuk-Jin Yoon. Scanline Resolution-Invariant Depth Completion Using A Single Image And Sparse LiDAR Point Cloud. *IRAL*, 6(4):6961–6968, 2021. 2

[33] Tim Salimans and Jonathan Ho. Progressive Distillation for Fast Sampling of Diffusion Models. In *ICLR*, 2021. 2

[34] Jiaming Song, Chenlin Meng, and Stefano Ermon. Denoising Diffusion Implicit Models. *arXiv preprint arXiv:2010.02502*, 2020. 3, 12

[35] Shuran Song, Fisher Yu, Andy Zeng, Angel X Chang, Manolis Savva, and Thomas Funkhouser. Semantic Scene Completion From A Single Depth Image. In *CVPR*, pages 1746–1754, 2017. 15

[36] Yang Song, Jascha Sohl-Dickstein, Diederik P Kingma, Abhishek Kumar, Stefano Ermon, and Ben Poole. Score-Based Generative Modeling through Stochastic Differential Equations. In *ICLR*, 2021. 16

[37] Yang Song, Prafulla Dhariwal, Mark Chen, and Ilya Sutskever. Consistency Models. In *ICML*, pages 32211–32252, 2023. 2, 12

[38] Ignacio Vizzo, Benedikt Mersch, Rodrigo Marcuzzi, Louis Wiesmann, Jens Behley, and Cyrill Stachniss. Make It Dense: Self-Supervised Geometric Scan Completion of Sparse 3d Lidar Scans In Large Outdoor Environments. *IRAL*, 7(3):8534–8541, 2022. 2, 6, 13, 15

[39] Fengyun Wang, Dong Zhang, Hanwang Zhang, Jinhui Tang, and Qianru Sun. Semantic Scene Completion With Cleaner Self. In *CVPR*, pages 867–877, 2023. 2

[40] Fu-Yun Wang, Ling Yang, Zhaoyang Huang, Mengdi Wang, and Hongsheng Li. Rectified diffusion: Straightness is not your need in rectified flow. *arXiv preprint arXiv:2410.07303*, 2024. 2

[41] Peihao Wang, Dejia Xu, Zhiwen Fan, Dilin Wang, Sreyas Mohan, Forrest Iandola, Rakesh Ranjan, Yilei Li, Qiang Liu, Zhangyang Wang, et al. Taming Mode Collapse In Score Distillation for Text-to-3d Generation. In *CVPR*, pages 9037–9047, 2024. 2

[42] Zhengyi Wang, Cheng Lu, Yikai Wang, Fan Bao, Chongxuan Li, Hang Su, and Jun Zhu. ProlificDreamer: High-Fidelity And Diverse Text-to-3D Generation With Variational Score Distillation. *NIPS*, 36:8406–8441, 2023. 2, 4, 16, 17

[43] Cho-Ying Wu and Ulrich Neumann. Scene Completeness-Aware Lidar Depth Completion For Driving Scenario. In *ICASSP*, pages 2490–2494, 2021. 2

[44] Zhaoyang Xia, Youquan Liu, Xin Li, Xinge Zhu, Yuexin Ma, Yikang Li, Yuenan Hou, and Yu Qiao. Scpnet: Semantic Scene Completion On Point Cloud. In *CVPR*, pages 17642–17651, 2023. 2

[45] Yuwen Xiong, Wei-Chiu Ma, Jingkang Wang, and Raquel Urtasun. Learning Compact Representations for Lidar Completion and Generation. In *CVPR*, pages 1074–1083, 2023. 11

[46] Yuwen Xiong, Wei-Chiu Ma, Jingkang Wang, and Raquel Urtasun. Learning Compact Representations For Lidar Completion and Generation. In *CVPR*, pages 1074–1083, 2023. 2

[47] Yan Xu, Xinge Zhu, Jianping Shi, Guofeng Zhang, Hujun Bao, and Hongsheng Li. Depth Completion from Sparse Lidar Data With Depth-Normal Constraints. In *ICCV*, pages 2811–2820, 2019. 2

[48] Yujie Xue, Ruihui Li, Fan Wu, Zhuo Tang, Kenli Li, and Mingxing Duan. Bi-SSC: Geometric-Semantic Bidirectional Fusion for Camera-based 3D Semantic Scene Completion. In *CVPR*, pages 20124–20134, 2024. 2

[49] Ling Yang, Zixiang Zhang, Zhilong Zhang, Xingchao Liu, Minkai Xu, Wentao Zhang, Chenlin Meng, Stefano Ermon, and Bin Cui. Consistency flow matching: Defining straight flows with velocity consistency. *arXiv preprint arXiv:2407.02398*, 2024. 2

[50] Yanchao Yang, Alex Wong, and Stefano Soatto. Dense Depth Posterior (DDP) From Single Image And Sparse Range. In *CVPR*, pages 3353–3362, 2019. 2

[51] Tianwei Yin, Michaël Gharbi, Taesung Park, Richard Zhang, Eli Shechtman, Fredo Durand, and Bill Freeman. Improved Distribution Matching Distillation For Fast Image Synthesis. *NIPS*, 37:47455–47487, 2024. 12

[52] Tianwei Yin, Michaël Gharbi, Richard Zhang, Eli Shechtman, Fredo Durand, William T Freeman, and Taesung Park. One-step Diffusion With Distribution Matching Distillation. In *CVPR*, pages 6613–6623, 2024. 4, 5, 12

[53] Qingyang Yu, Lei Chu, Qi Wu, and Ling Pei. Grayscale And Normal Guided Depth Completion With A Low-cost LiDAR. In *ICIP*, pages 979–983, 2021. 2

[54] Shengyuan Zhang, Ling Yang, Zejian Li, An Zhao, Chenye Meng, Changyuan Yang, Guang Yang, Zhiyuan Yang, and Lingyun Sun. Distribution Backtracking Builds A Faster Convergence Trajectory for One-step Diffusion Distillation. In *ICLR*, 2025. 2, 5, 12

[55] Linqi Zhou, Yilun Du, and Jiajun Wu. 3d Shape Generation And Completion Through Point-voxel Diffusion. In *ICCV*, pages 5826–5835, 2021. 6, 15

A. Experiment protocol

A.1. Dataset setup

SemanticKITTI [1] dataset is a large-scale benchmark for 3D semantic segmentation in autonomous driving, extending the KITTI Odometry dataset with dense semantic annotations for over 43,000 LiDAR scans. It provides labels for 25 classes, such as “car,” “road,” and “building,” capturing diverse urban and rural scenes. The SemanticKITTI dataset consists of 22 sequences, where sequences 00-10 are densely annotated for each scan, enabling tasks such as semantic segmentation and semantic scene completion using sequential scans. Sequences 11-21 serve as the test set, showcasing diverse and challenging traffic situations and environment types to evaluate model performance in real-world autonomous driving scenarios. SemanticKITTI is widely used in research and serves as a critical resource for advancing LiDAR-based perception systems.

KITTI-360 [20] dataset is a comprehensive benchmark for 3D scene understanding in autonomous driving, capturing 360-degree panoramic imagery and 3D point clouds across diverse urban environments. It includes over 73 km of driving data with dense semantic annotations for both 2D (images) and 3D (point clouds), covering categories like “vehicles,” “buildings,” and “vegetation.” KITTI-360 provides high-resolution sensor data, including LiDAR, GPS/IMU, and stereo camera recordings, making it ideal for tasks such as 3D semantic segmentation, panoptic segmentation, and mapping in real-world driving scenarios.

A.2. Evaluation metrics

Chamfer Distance (CD) [2] is a metric used to measure the similarity between two sets of points, often employed for evaluating the quality of generated point clouds or geometric shapes. For two point sets P and Q , the Chamfer Distance is defined as:

$$CD(P, Q) = \frac{1}{|P|} \sum_{p \in P} \min_{q \in Q} \|p - q\|^2 + \frac{1}{|Q|} \sum_{q \in Q} \min_{p \in P} \|q - p\|^2 \quad (19)$$

The first term calculates the average squared distance from each point in P to its nearest neighbour in Q . The second term calculates the average squared distance from each point in Q to its nearest neighbour in P . Chamfer Distance evaluates how well two point sets approximate each other by considering their nearest neighbour distances in both directions. CD effectively captures local geometric features and exhibits strong robustness in local shape matching, which is commonly used in evaluating the matching and reconstruction of 3D point clouds.

Jensen-Shannon Divergence (JSD) [24] is a symmetric measure of similarity between two probability distributions.

It is a variation of the Kullback-Leibler (KL) divergence and is widely used in information theory, statistics, and machine learning. Given two probability distributions P and Q over the same domain, JSD is defined as:

$$JSD(P||Q) = \frac{1}{2} KL(P||M) + \frac{1}{2} KL(Q||M) \quad (20)$$

Here $M = \frac{1}{2}(P + Q)$ is the average distribution, and $KL(P||M)$ is the Kullback-Leibler divergence.

JSD measures how much P and Q diverge from their average distribution M . It is symmetric ($JSD(P||Q) = JSD(Q||P)$) and always produces a finite value in the range $[0, 1]$ when using base-2 logarithms. Unlike KL divergence, JSD avoids issues with undefined values when probabilities are zero in one of the distributions. JSD is an efficient metric to evaluate the similarity between two distributions. The calculation of JSD in this paper is followed by Xiong *et al.* [45].

A.3. Implementation details

We choose the pre-trained LiDiff [28] model as the teacher model ϵ_θ , the student model G_{stu} and the auxiliary diffusion model ϵ_ϕ shares the same network architecture as the teacher model and are initialized by the teacher model. The ScoreLiDAR is trained on SemanticKITTI dataset. The pre-trained diffusion model is provided by the official release of LiDiff [28]. For fair comparison, we follow LiDiff [28]’s training strategy. ScoreLiDAR is trained on sequences 00-07 and 09-10 of SemanticKITTI (does not train on KITTI-360), and evaluated on sequence 08 of SemanticKITTI and sequence 00 of KITTI-360.

For optimization, we use the Stochastic Gradient Descent (SGD) optimizer with the default parameters. The learning rate is set to $3e-5$ and the batch size is set to 1. The training ratio between the student model and the auxiliary diffusion model is maintained at 1 : 1. To reduce computational costs, when calculating the point-wise loss, we first randomly select $\frac{1}{10}$ of the points from the ground truth scene. Then, following the proposed method, we select the top $\frac{1}{3}$ points with the highest curvature from these points as the key points to calculate the distance matrix. That is, the final number of key points is $\frac{1}{30}$ of the total number of points in the ground truth scene. When calculating the K -nearest neighbours, we set $K = 180$. The weights of scene-wise loss λ_{scene} and the point-wise loss λ_{point} are set to 0.5 and 0.01, respectively. ScoreLiDAR requires only 50 iterations to achieve convergence, taking approximately 10 minutes on a single A40 GPU, which is highly efficient. Our model and code are publicly available on <https://github.com/happyw1nd/ScoreLiDAR>.

B. Discussion

B.1. The effectiveness of the distillation on improving the completion efficiency

In this part, we provide a detailed discussion about the efficiency of the proposed distillation method.

Why is it reasonable to initialize the student model and auxiliary diffusion model using the teacher model?

Firstly, such an initialization method is commonly used in existing methods [22, 37, 51, 52, 54]. Secondly, the pre-trained teacher model ϵ_θ contains the information about the training distribution, initializing the student model with the teacher model to perform distillation is essentially a fine-tuning process for the teacher model, which can accelerate the efficiency of the distillation. Third, although the student model has the same parameters and the network structure as the teacher model, its sampling distribution is different from that of the teacher model due to the different sampling steps. The teacher model ϵ_θ (LiDiff [28] in this case) conducts the multi-step sampling.

$$\mathcal{G}^{t-1} = \frac{1}{\sqrt{\alpha^t}} \left(\mathcal{G}^t - \frac{1 - \alpha^t}{\sqrt{1 - \bar{\alpha}^t}} \epsilon_\theta(\mathcal{G}^t, \mathcal{P}, t) \right) + \sigma^t \mathbf{z} \quad (21)$$

The teacher model ϵ_θ from LiDiff [28] conducts 50-steps sampling by repeating Eq. (21). The student model G_{stu} conducts the single-step sampling. After G_{stu} predicts the noise, a single-step denoising in Eq. (22) is performed to directly obtain the completed scene \mathcal{G}^0 .

$$\mathcal{G}^0 = \frac{1}{\sqrt{\alpha^t}} \left(\mathcal{G}^t - \frac{1 - \alpha^t}{\sqrt{1 - \bar{\alpha}^t}} \epsilon_\theta(\mathcal{G}^t, \mathcal{P}, t) \right) \quad (22)$$

Thus, the single-step sampling scene of the student model is different from the multi-step sampling scene of the teacher model.

Why is the distillation loss effective? Why does the student model get optimized? Firstly, our distillation loss is different from the standard loss of the diffusion models such as DDPM [10]. The loss of DDPM is to directly predict the noise added to the training sample. Differently, in proposed ScoreLiDAR, the distillation loss utilizes the noise predicted by the student model G_{stu} to perform a one-step sampling, resulting in a completed scene \mathcal{G}^0 different from the multi-step sampling of the teacher model. The completed scene \mathcal{G}^0 is then perturbed noise on a random timestep t to obtain the noisy scene \mathcal{G}^t , and the difference between two score functions according to \mathcal{G}^t is calculated to serve as the gradient for optimizing the student model, as shown in Eq. (23)

$$\mathcal{L}_{KL} \approx \mathbb{E}_{t, \epsilon} [\|\epsilon_\theta(\mathcal{G}^t, \mathcal{P}, t) - \epsilon_\phi(\mathcal{G}^t, \mathcal{P}, t)\|_2^2] \quad (23)$$

Secondly, although the auxiliary diffusion model ϵ_ϕ is initialized from the teacher model ϵ_θ , the gradient in Eq. (23) is non-zero and efficient. Recall that the auxiliary diffusion model ϵ_ϕ and the student model G_{stu} are trained alternately. The auxiliary diffusion model ϵ_ϕ is first trained on \mathcal{G}^0 to fit the one-step sampling distribution, which is different from the pre-trained distribution of the teacher model. Although the auxiliary diffusion model ϵ_ϕ is also initialized from the teacher model, its parameter will be updated and become different from the teacher model's after one optimization. Then, when G_{stu} is optimized using the gradient in Eq. (23), the output of $\epsilon_\theta(\mathcal{G}^t, \mathcal{P}, t)$ is naturally different from the output of $\epsilon_\phi(\mathcal{G}^t, \mathcal{P}, t)$ due to the optimization of ϵ_ϕ . Thus, as mentioned in Sec. 4.1 of the main paper, the non-zero gradient in Eq. (23) will optimize the distribution of G_{stu} moving towards the pre-trained distribution of the teacher model. Then, ϵ_ϕ and G_{stu} are optimized in turn to convergence.

Why is one-step sampling used during training, while few-step sampling is used during inference? Firstly, in traditional diffusion models like DDPM [10] and DDIM [34], they directly predict the whole noise added in the diffusion process during the training, whereas a multi-step sampling process is performed during sampling. Meanwhile, different sampling methods allow for sampling with different numbers of steps. Intuitively, this indicates that although the training objective remains the same, the sampling can be performed with different numbers of steps. A more profound explanation is from solving the stochastic differential equation as in the diffusion model. Moreover, Consistency Model [37] also has a similar setting; its student model performs one-step generation during training but conducts multi-step generation during sampling. We adopted a similar principle as in the Consistency Model. The one-step sampling in our training is to increase the fidelity of the resulting sample given different noisy samples, while in inference multi-step sampling would gradually refine the final result. Therefore, although the student model performs one-step sampling during training, the quality of scene completion can be improved by increasing the number of sampling steps during the inference. More visually, the one-step generation procedure of the Consistency Model is “noise→image”, and the multi-step generation procedure is “noise→noisy image→…→image”. In this paper, the one-step sampling of student model G_{stu} during training is “noise→predicted noise→completed scene” and the few-step sampling during inference is “noise→predicted noise→noisy scene→predicted noise→noisy scene→predicted noise→…→completed scene”. In summary, it is reasonable to use one-step sampling during training and multi-step sampling during inference.

B.2. The different of scene-wise loss and Chamfer Distance

The scene-wise loss has the following form

$$\mathcal{L}_{scene} = \frac{1}{|\mathcal{G}^0|} \sum_{p_i^0 \in \mathcal{G}^0} \min_{p \in \mathcal{G}} \|p_i^0 - p\|^2 \quad (24)$$

The scene-wise loss is part of the Chamfer Distance. The reason for using only part of the Chamfer Distance (CD) is that the optimization objective of scene-wise loss is to ensure that the points in the generated scene \mathcal{G}^0 are as close as possible to the corresponding points in the ground truth. The unused term in CD matches each point in ground truth with its nearest point in generated scene \mathcal{G}^0 , which may lead to points in \mathcal{G}^0 being pushed toward the average position of non-existent matching points in the ground truth. This effect is detrimental to scene completion.

B.3. Discussion on the significance of this study

Firstly, we discuss the significance of this study. For autonomous vehicles, accurately recognizing and perceiving their surrounding environment during operation is critical [17, 18]. This is particularly important for identifying objects that may affect the vehicle’s movement, such as other vehicles, pedestrians, traffic cones, and signposts [12]. The accurate and efficient recognition of these objects is essential for the safe operation of autonomous vehicles. However, the scan data obtained by onboard LiDAR is sparse [16, 38], and it is difficult to identify key objects such as vehicles from the magnified regions of the sparse scan. Autonomous vehicles cannot obtain sufficient information about the driving environment from these sparse LiDAR scans [14, 29]. Therefore, it is necessary to use appropriate methods to complete the sparse LiDAR scans.

LiDiff [28] uses DDPM [10] models to complete 3D LiDAR scenes, achieving impressive results. However, due to the inherent characteristics of diffusion models, LiDiff [28] requires approximately 30 seconds to complete a single scene, limiting its applicability in autonomous vehicles. In contrast, the proposed ScoreLiDAR can complete a scene in almost 5 seconds, more than 5 times faster than LiDiff [28], while achieving higher completion quality. Thus, with the scenes completed by the proposed ScoreLiDAR, autonomous vehicles can more easily recognize critical objects in their driving environment, enabling safer and more effective navigation.

C. Additional completed scenes

Fig. 7 and Fig. 8 show additional completed scenes by the proposed ScoreLiDAR and compare them with the scenes completed by LiDiff [28].

Model	SemanticKITTI			KITTI360		
	CD ↓	JSD ↓	EMD ↓	CD ↓	JSD ↓	EMD ↓
ScoreLiDAR	0.342	0.399	23.26	0.452	0.437	23.02
w/o Point-wise loss	0.351	0.414	23.37	0.485	0.486	23.29
w/o Scene-wise loss	0.367	0.422	24.89	0.477	0.451	24.69
w/o Structural Loss	0.419	0.430	24.13	0.549	0.445	24.56

Table 5. Ablation study of the scene-wise and point-wise loss. The metrics refer to the performance with refinement. Colors denote the 1st, 2nd, and 3rd best-performing model.

Model	SemanticKITTI			KITTI360		
	CD ↓	JSD ↓	EMD ↓	CD ↓	JSD ↓	EMD ↓
$\lambda_{scene} = 0.5, \lambda_{point} = 0.01$	0.342	0.399	23.26	0.452	0.437	23.02
$\lambda_{scene} = 0.05, \lambda_{point} = 0.01$	0.354	0.409	23.40	0.494	0.457	23.21
$\lambda_{scene} = 0.5, \lambda_{point} = 0.1$	0.358	0.419	23.27	0.539	0.474	23.09

Table 6. Ablation study of the different weights of the scene-wise and point-wise loss. The first row refers to the default configuration of the ScoreLiDAR. The metrics refer to the performance with refinement.

Model	SemanticKITTI		KITTI360	
	CD ↓	JSD ↓	CD ↓	JSD ↓
LiDiff (Refined)	0.375	0.416	0.517	0.446
w/ Structural loss	0.399	0.426	0.535	0.450

Table 7. Ablation study of training LiDiff [28] with structural loss.

D. Additional experiment results

D.1. More ablation study of structural loss

To further validate the effectiveness of the structural loss, we evaluated the performance of variants trained with only point-wise loss or scene-wise loss and compared them with default ScoreLiDAR. As shown in Tab. 5, compared to the default ScoreLiDAR, the performance of variants trained with only scene-wise loss or point-wise loss decreased. However, compared to the variants without structural loss, the variants using only one type of loss still showed improved completion performance. These results confirm the effectiveness of the structural loss in the distillation process.

Additionally, we investigated the impact of different weights of scene-wise and point-wise loss on the completion quality. The results are shown in Tab. 6. It can be observed that reducing λ_{scene} or increasing λ_{point} leads to a decline in the performance of ScoreLiDAR but still achieves a comparable performance. This verifies the effectiveness of the proposed structural loss in improving the completion performance of the student model.

Finally, we trained LiDiff using structural loss to investigate whether structural loss can enhance the performance of LiDiff. The results are shown in Tab. 7. Training LiDiff [28] with structural loss does not result in a performance

ScoreLiDAR	SemanticKITTI			KITTI360		
	CD ↓	JSD ↓	EMD ↓	CD ↓	JSD ↓	EMD ↓
$n = 1/20$	0.329	0.392	24.35	0.528	0.475	24.01
$n = 1/30$	0.342	0.399	23.26	0.452	0.437	23.02
$n = 1/60$	0.346	0.409	25.19	0.452	0.471	25.05
$n = 1/70$	0.428	0.454	25.60	0.466	0.479	25.44

Table 8. Ablation study of different key points number. The result of $n = 1/30$ refers to the default configuration of the ScoreLiDAR. The metrics refer to the performance with refinement.

Model	CD ↓	JSD ↓	EMD ↓
Random selection	0.384	0.433	23.23
farthest selection	0.442	0.459	23.63
ScoreLiDAR	0.342	0.399	23.26

Table 9. Comparison of different selection methods on SemanticKITTI dataset. The performance of the proposed selection method is better than others.

improvement. This may be because structural loss is not suitable for direct addition to the training loss of LiDiff [28], *i.e.* the traditional diffusion model training loss.

D.2. Ablation study of different key point number

As mentioned in Appendix A.3, the optimal number of the key point is set to the $\frac{1}{30}$ of the total number of points in the ground truth. To investigate the impact of different numbers of key points on the completion performance of ScoreLiDAR, we decreased the number of key points for model training and evaluated the completion performance. As shown in Tab. 8, the final performance of ScoreLiDAR is positively correlated with the number of key points. When the number of key points decreases, the performance of ScoreLiDAR declines. This is because an insufficient number of key points causes the point-wise loss to fail in effectively capturing the relative positional information between key points, preventing the student model from learning the local geometric structure, and thereby reducing the completion quality. However, when the number of key points is too large, it can easily cause an out-of-memory issue and reduce training efficiency. Therefore, this paper sets $n = \frac{1}{30}$.

D.3. Ablation study of different key point selection method

We compare different key point selection methods including random selection and farthest selection with the proposed selection method based on curvature. The results in Tab. 9 show that using the proposed selection method based on curvature achieves the optimal performance than other selection methods.

Model	CD ↓	JSD ↓	EMD ↓	Time (s) ↓
LiDiff (50 steps) [28]	0.564	0.549	21.98	29.18
LiDiff (50 steps Refined) [28]	0.517	0.446	22.96	29.43
LiDiff (8 steps) [28]	0.619	0.471	24.85	5.46
LiDiff (8 steps Refined) [28]	0.550	0.462	25.49	5.77
ScoreLiDAR (8 Steps)	0.452	0.437	23.02	5.14
ScoreLiDAR (4 Steps)	0.482	0.461	23.76	3.16
ScoreLiDAR (2 Steps)	0.525	0.457	-	1.69
ScoreLiDAR (1 Steps)	0.750	0.478	-	1.03

Table 10. Ablation study of different sampling steps on the KITTI-360 dataset. The metrics of ScoreLiDAR refer to the performance with refinement.

Model	User preference ↑
LiDiff [28]	35%
ScoreLiDAR	65%

Table 11. Results of user study. Our ScoreLiDAR outperforms the existing SOTA model.

D.4. Ablation study of different sampling steps on KITTI-360

We also conduct the ablation study of different sampling steps on the KITTI-360 dataset. The results are shown in Tab. 10. Similar to the results on the SemanticKITTI dataset, as the number of sampling steps decreases, the time required for ScoreLiDAR to complete a scene is reduced. Although the completion performance declines slightly, it remains comparable to that of existing SOTA models.

D.5. User study

The user study is conducted to verify the completion performance of ScoreLiDAR further. We first used ScoreLiDAR and the current SOTA method LiDiff [28] to complete the same 30 input LiDAR scans, resulting in 30 pairs of completed scenes. We then randomly recruited seven volunteers and guided each to evaluate the detail and fidelity of these 30 pairs of scene images, selecting the one they believed to be closer to the ground truth. The seven volunteers included five men and two women, aged 24–30, with five participants having research backgrounds related to autonomous driving or LiDAR scene completion and the remaining two participants having backgrounds related to artificial intelligence. They were given unlimited time for the evaluation, but the average completion time for all volunteers was 30 minutes.

The result of the user study is shown in Tab. 11. Compared to LiDiff, ScoreLiDAR received a 65% user preference, surpassing the majority threshold. This indicates that, in the eyes of most users, the detail and fidelity of the scenes completed by ScoreLiDAR more closely resemble the ground truth. The results of the user study further demonstrate the effectiveness of ScoreLiDAR in LiDAR

Model	SemanticKITTI (IoU) % ↑		
	0.5m	0.2m	0.1m
LMSCNet [30]	32.23	23.05	3.48
LODE [16]	43.56	47.88	6.06
MID [38]	45.02	41.01	16.98
PVD [55]	21.20	7.96	1.44
LiDiff [28]	42.49	33.12	11.02
LiDiff (Refined) [28]	40.71	38.92	24.75
ScoreLiDAR	38.43	25.75	8.34
ScoreLiDAR (Refined)	37.33	29.57	15.63

Table 12. The IoU evaluation results on the SemanticKITTI dataset.

Model	KITTI-360 (IoU) % ↑		
	0.5m	0.2m	0.1m
LMSCNet [30]	25.46	16.35	2.99
LODE [16]	42.08	42.63	5.85
MID [38]	44.11	36.38	15.84
LiDiff [28]	42.22	32.25	10.80
LiDiff (Refined) [28]	40.82	36.08	21.34
ScoreLiDAR	36.82	25.49	9.70
ScoreLiDAR (Refined)	33.29	28.60	15.95

Table 13. The IoU evaluation results on the KITTI-360 dataset.

scene completion.

D.6. Visualization of key points

To validate the feasibility of our proposed key point selection method, we visualized the selected key points in the ground truth scene. As shown in Fig. 6, the red key points are mostly distributed on walls, traffic cones, cars, and corners, while smooth areas such as the road surface have no key points. These key points are crucial for expressing the details of 3D LiDAR scenes. Selecting these points to compute the point-wise loss allows the student model to more easily capture the relative configuration information between key points, thereby better completing key objects in the scene.

D.7. Experiments on semantic scene completion

The objective of this paper is to propose a foundational method for distillation acceleration applicable to various LiDAR scene completion diffusion models. Semantic scene completion is not within the scope of the fundamental experiments considered in this paper. In spite of this, to validate the generalizability of the proposed method, we use SemCity [15] as the teacher model to verify the effectiveness of ScoreLiDAR on semantic scene completion tasks. Because the pre-trained models and code for the

Model	FID ↓	KID ↓
SemCity [15]	88.52	0.11
ScoreLiDAR	81.76	0.09

Table 14. Results of semantic scene completion. Our ScoreLiDAR shows better performance.

metric computation of SemCity are not publicly available, we retrained SemCity based on the official implementation and reproduced the metric computation ourselves. Tab. 14 shows the results. In semantic scene completion tasks, the proposed ScoreLiDAR still shows better completion quality than that of the teacher model.

D.8. Experiments on scene occupancy

We calculate the Intersection-Over-Union (IoU) [35] to evaluate the occupancy of the completed scene compared with the ground truth scene. IoU represents the degree of overlap between the voxels in the completed scene and those in the ground truth scene. A higher IoU value indicates a higher completeness of the completed scene. During the evaluation, we considered three different voxel resolutions: 0.5m, 0.2m, and 0.1m. The smaller the voxel resolution, the more fine-grained details are considered in the evaluation metrics, and vice versa. However, IoU is a voxel-based metric, and in some voxel-based LiDAR scene completion methods, it can serve as an accurate measure of completion quality. In contrast, ScoreLiDAR is a point cloud-based completion method, which differs from traditional voxel-based approaches. As a result, IoU may introduce bias when evaluating the completion quality. Therefore, here we provide IoU results solely as a relative reference.

Tab. 12 and Tab. 13 show the IoU of ScoreLiDAR and existing models. Under low voxel resolutions, ScoreLiDAR achieves comparable IoU values, meaning ScoreLiDAR generates dense and accurate point clouds. When the voxel resolutions become higher, the performance of ScoreLiDAR declines. As mentioned above, the existing method is mainly based on signed distance fields, which implement the scene completion using a voxel representation. ScoreLiDAR is point-level scene completion with the input of point clouds obtained from LiDAR scans, which works better at smaller voxel resolutions.

E. Theoretical demonstration

The gradient of the student model is Eq. (25).

$$\begin{aligned} & \nabla_{\eta} D_{\text{KL}}(p_G^t(\mathcal{G}^t) \| q^t(\mathcal{G}^t)) \\ &= \mathbb{E}_{t, \epsilon} [\nabla_{\mathcal{G}^t} \log p_G^t(\mathcal{G}^t) - \nabla_{\mathcal{G}^t} \log q^t(\mathcal{G}^t)] \frac{\partial \mathcal{G}^t}{\partial \eta} \end{aligned} \quad (25)$$

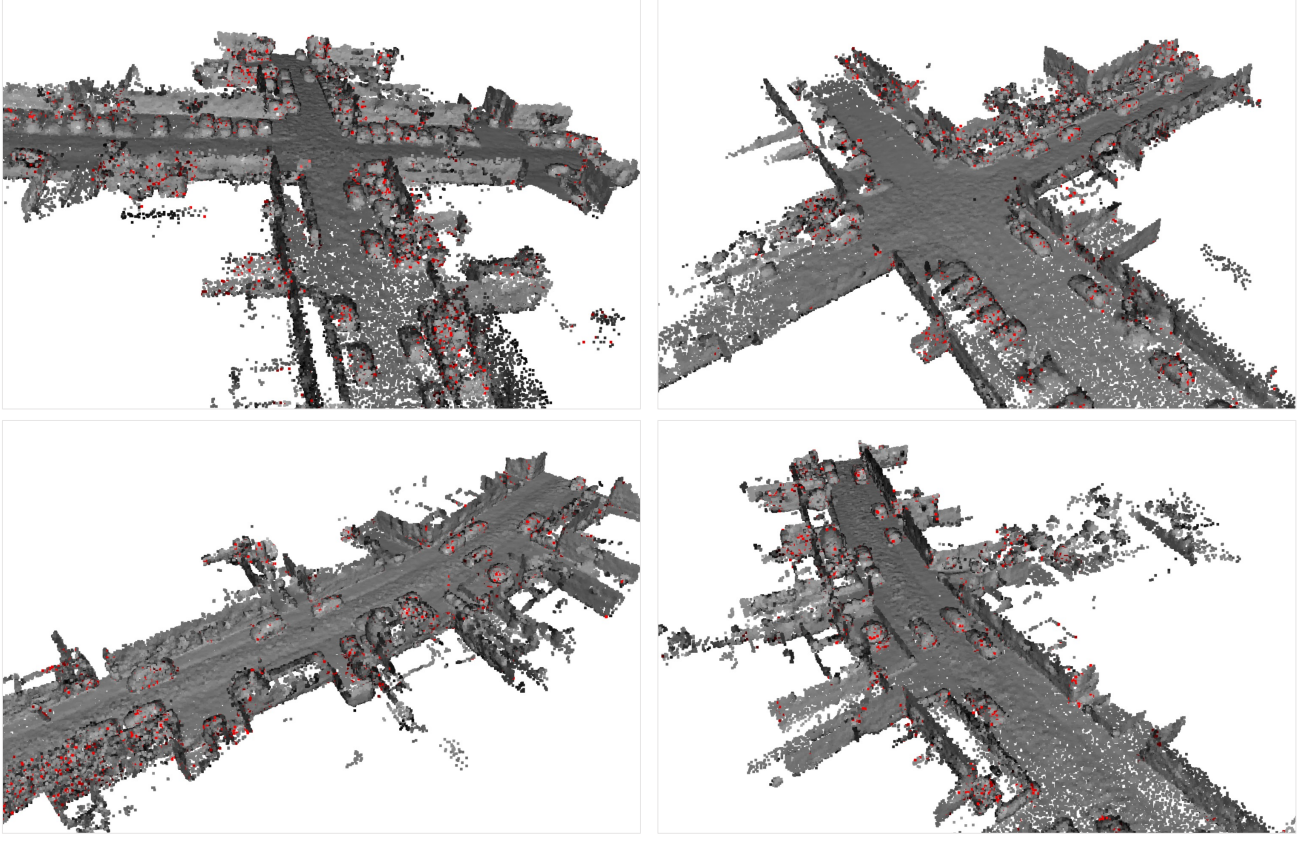


Figure 6. The visualization of the selected key points. Red points refer to the key points selected by the proposed method.

As proposed in ScoreSDE [36], the log likelihood $\nabla_{\mathcal{G}^t} \log q^t(\mathcal{G}^t)$ can be approximated by the predicted noise $\hat{\epsilon}$ with $\nabla_{\mathcal{G}^t} \log q^t(\mathcal{G}^t) \approx -\frac{\hat{\epsilon}}{\sqrt{1-\bar{\alpha}^t}}$. Thus, the gradient in Eq. (25) can be written as

$$\begin{aligned} & \nabla_{\eta} D_{\text{KL}}(p_G^t(\mathcal{G}^t) \| q^t(\mathcal{G}^t)) \\ &= \mathbb{E}_{t,\epsilon} \left[\nabla_{\mathcal{G}^t} \log p_G^t(\mathcal{G}^t) - \nabla_{\mathcal{G}^t} \log q^t(\mathcal{G}^t) \right] \frac{\partial \mathcal{G}^t}{\partial \eta} \\ & \approx \mathbb{E}_{t,\epsilon} \left[-\frac{\epsilon_{\phi}(\mathcal{G}^t, \mathcal{P}, t)}{\sqrt{1-\bar{\alpha}^t}} - \left(-\frac{\epsilon_{\theta}(\mathcal{G}^t, \mathcal{P}, t)}{\sqrt{1-\bar{\alpha}^t}} \right) \right] \frac{\partial \mathcal{G}^t}{\partial \eta} \quad (26) \\ &= \mathbb{E}_{t,\epsilon} \left[\frac{\epsilon_{\theta}(\mathcal{G}^t, \mathcal{P}, t)}{\sqrt{1-\bar{\alpha}^t}} - \frac{\epsilon_{\phi}(\mathcal{G}^t, \mathcal{P}, t)}{\sqrt{1-\bar{\alpha}^t}} \right] \frac{\partial \mathcal{G}^t}{\partial \eta} \end{aligned}$$

Here $\sqrt{1-\bar{\alpha}^t}$ can be ignored. Thus, the gradient of G_{stu} can be approximated by

$$\begin{aligned} & \nabla_{\eta} D_{\text{KL}}(p_G^t(\mathcal{G}^t) \| q^t(\mathcal{G}^t)) \\ & \approx \mathbb{E}_{t,\epsilon} \left[\epsilon_{\theta}(\mathcal{G}^t, \mathcal{P}, t) - \epsilon_{\phi}(\mathcal{G}^t, \mathcal{P}, t) \right] \frac{\partial \mathcal{G}^t}{\partial \eta} \quad (27) \end{aligned}$$

F. Introduction on utilized methods

F.1. Variational score distillation

Variational Score Distillation (VSD), proposed by ProlificDreamer [42], is designed to leverage a pre-trained diffusion model to train a NeRF [26], enabling the rendering of high-quality 3D objects.

Given a text prompt y , the probabilistic distribution of all possible 3D representations can be modeled as a probabilistic density $\mu(\theta|y)$ by a NeRF model parameterized by θ . Let $q_0^{\mu}(\mathbf{x}_0|c, y)$ as the distribution of the rendered image \mathbf{x}_0 of NeRF given the camera c , and $p_0(\mathbf{x}_0|y)$ as the distribution of the pre-trained text-to-image diffusion model at $t = 0$. To generate high-quality 3D objects, ProlificDreamer [42] optimizes the distribution of μ by minimizing the following KL divergence

$$\min_{\mu} D_{\text{KL}}(q_0^{\mu}(\mathbf{x}_0|y) \| p_0(\mathbf{x}_0|y)) \quad (28)$$

However, directly solving this variational inference problem is challenging because p_0 is complex, and its high-density regions may be extremely sparse in high-dimensional spaces. Therefore, ProlificDreamer reformu-

lates it as an optimization problem at different time steps t , referring to these problems as Variational Score Distillation (VSD),

$$\min_{\mu} \mathbb{E}_{t,c} [(\sigma_t/\alpha_t) \omega(t) D_{\text{KL}} (q_t^{\mu}(\mathbf{x}_t | c, y) \| p_t(\mathbf{x}_t | y))] \quad (29)$$

Theorem 1 in [42] proves that introducing the additional t does not affect the global optimum of Eq. (28). Theorem 2 in [42] provides the method for optimizing the problem in Eq. (29).

$$\begin{aligned} \frac{d\theta_{\tau}}{d\tau} = & -\mathbb{E}_{t,\epsilon,c} [\omega(t) \underbrace{(-\sigma_t \nabla_{\mathbf{x}_t} \log p_t(\mathbf{x}_t | y))}_{\text{score of noisy real images}} \\ & - \underbrace{(-\sigma_t \nabla_{\mathbf{x}_t} \log q_t^{\mu\tau}(\mathbf{x}_t | c, y))}_{\text{score of noisy rendered images}} \frac{\partial \mathbf{g}(\theta_{\tau}, c)}{\partial \theta_{\tau}}] \end{aligned} \quad (30)$$

Here the score of noisy real images is approximated by the pre-trained diffusion model $\epsilon_{\text{pretrain}}(\mathbf{x}_t, t, y)$ and the score of noisy rendered images is approximated by another diffusion model $\epsilon_{\phi}(\mathbf{x}_t, t, c, y)$, which is trained on the rendered images with the standard diffusion objective.

$$\min_{\phi} \sum_{i=1}^n \mathbb{E}_{t,\epsilon,c} \left[\left\| \epsilon_{\phi} \left(\alpha_t \mathbf{g}(\theta^{(i)}, c) + \sigma_t \epsilon, t, c, y \right) - \epsilon \right\|_2^2 \right] \quad (31)$$

In practice, $\epsilon_{\phi}(\mathbf{x}_t, t, c, y)$ is parameterized by a small UNet or the Low-rank adaptation (LoRA) [11] of the teacher model. With the alternating training of NeRF and $\epsilon_{\phi}(\mathbf{x}_t, t, c, y)$, ProlificDreamer [42] is ultimately able to generate high-quality 3D objects.

F.2. MinkowskiEngine

Sparse tensor computation plays a critical role in fields such as 3D point cloud processing, computer vision, and physical simulations. Unlike dense tensors, sparse tensors contain a high proportion of zero values and directly applying traditional tensor operations can lead to inefficient use of computational resources. Minkowski Engine [5] addresses these challenges by providing a high-performance framework tailored for sparse tensor computation, enabling efficient operations on high-dimensional sparse data. In this paper, we used the Minkowski Engine to process sparse point cloud data.

Minkowski Engine introduces several innovative approaches to sparse tensor processing.

- Efficient Sparse Tensor Representation. Sparse tensors are represented using coordinate-value pairs, eliminating the need to store zeros. This representation reduces both memory usage and computational overhead.
- Sparse Convolution Operations The framework supports high-dimensional sparse convolutions, with kernels designed to adapt to varying sparsity patterns. Optimized

memory access patterns and parallel computation strategies ensure high efficiency.

- Fast Coordinate Mapping Minkowski Engine employs hash tables for rapid coordinate mapping, which accelerates tensor indexing and sparse pattern matching.
- Automatic Differentiation Support The framework includes built-in support for automatic differentiation, facilitating the training of machine learning models based on sparse tensors.
- Multi-Dimensional Capability Minkowski Engine can handle sparse tensors of arbitrary dimensions, making it suitable for a wide range of applications, from 2D image processing to 5D simulations.

Minkowski Engine has been widely adopted in various domains including 3D point cloud processing, physical simulations and medical imaging. By significantly improving computational efficiency and scalability, the Minkowski Engine has become a preferred choice for handling sparse tensor computations in both research and industrial applications.

G. Ethical statement

The potential ethical impact of our work is about fairness. As “human” is included as a kind of object in the LiDAR scene, when performing scene completion, it may be necessary to complete human figures. Human-related objects may have data bias related to fairness issues, such as the bias to gender or skin colour. Such bias can be captured by the student model in the training.

G.1. Notification to human subjects

In our user study, we present the notification to subjects to inform the collection and use of data before the experiments.

Dear volunteers, we would like to thank you for supporting our study. We propose ScoreLiDAR, a novel distillation method tailored for 3D LiDAR scene completion, which introduces a structural loss to help the student model capture the geometric structure information. All information about your participation in the study will appear in the study record. All information will be processed and stored according to the local law and policy on privacy. Your name will not appear in the final report. Only an individual number assigned to you is mentioned when referring to the data you provided.

We respect your decision whether you want to be a volunteer for the study. If you decide to participate in the study, you can sign this informed consent form.

The Institutional Review Board approved the use of users' data of the main authors' affiliation.

H. Failure examples

Fig. 9 presents some failure cases of ScoreLiDAR. From these examples, it can be observed that ScoreLiDAR exhibits over-completion to some extent, where regions that do not exist are completed. Before the completion, as mentioned in Sec.3 in the main paper, the number of points of the input sparse scan \mathcal{P} is increased by concatenating its points K times and the dense input \mathcal{P}^* is obtained. If the number of points of \mathcal{P}^* exceeds the actual number of points in the ground truth, it can lead to redundant points in the completed scene. These redundant points may be distributed in areas that do not require completion, resulting in the situations observed in the failure cases.

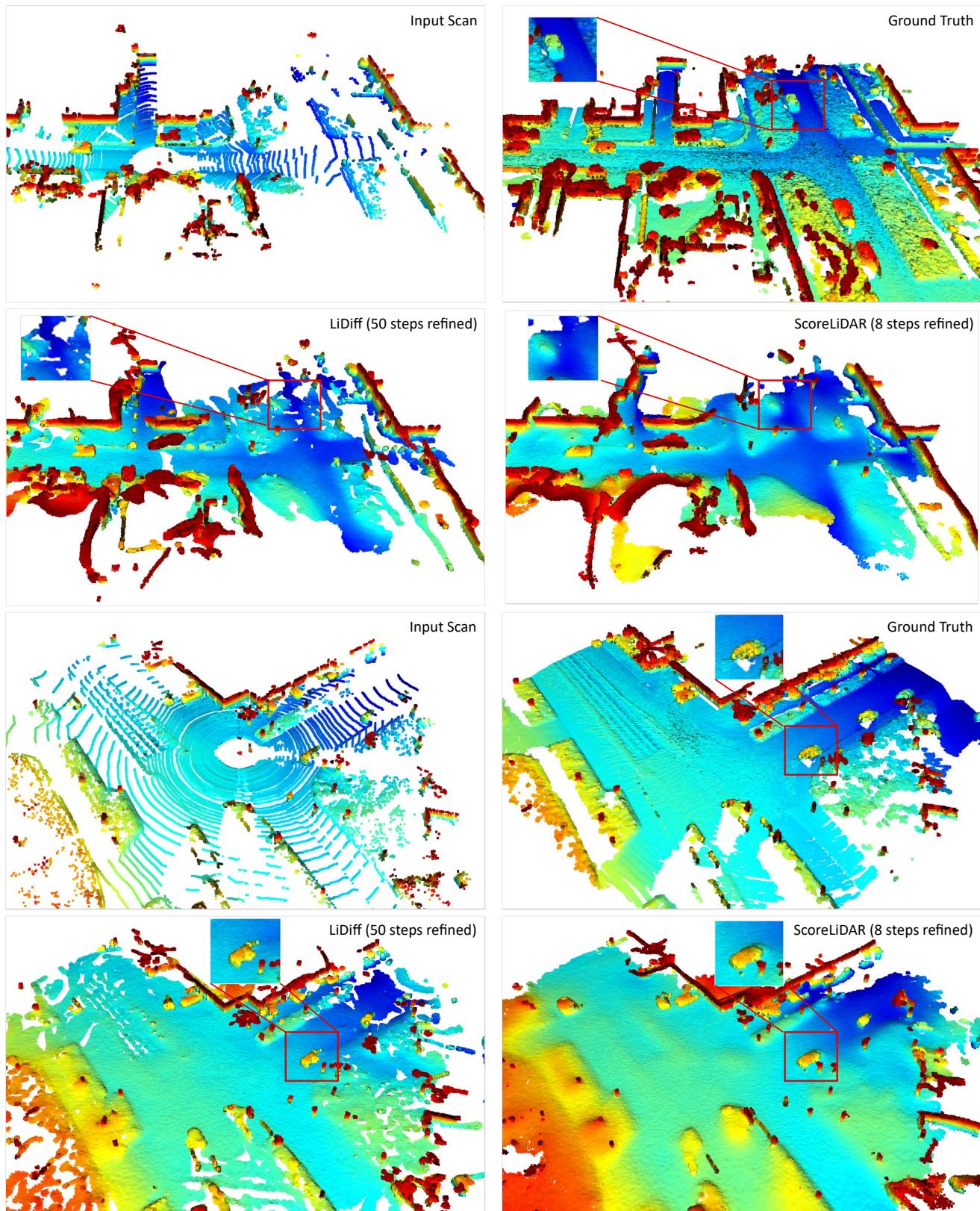


Figure 7. Completed samples of ScoreLiDAR from KITTI-360 dataset.

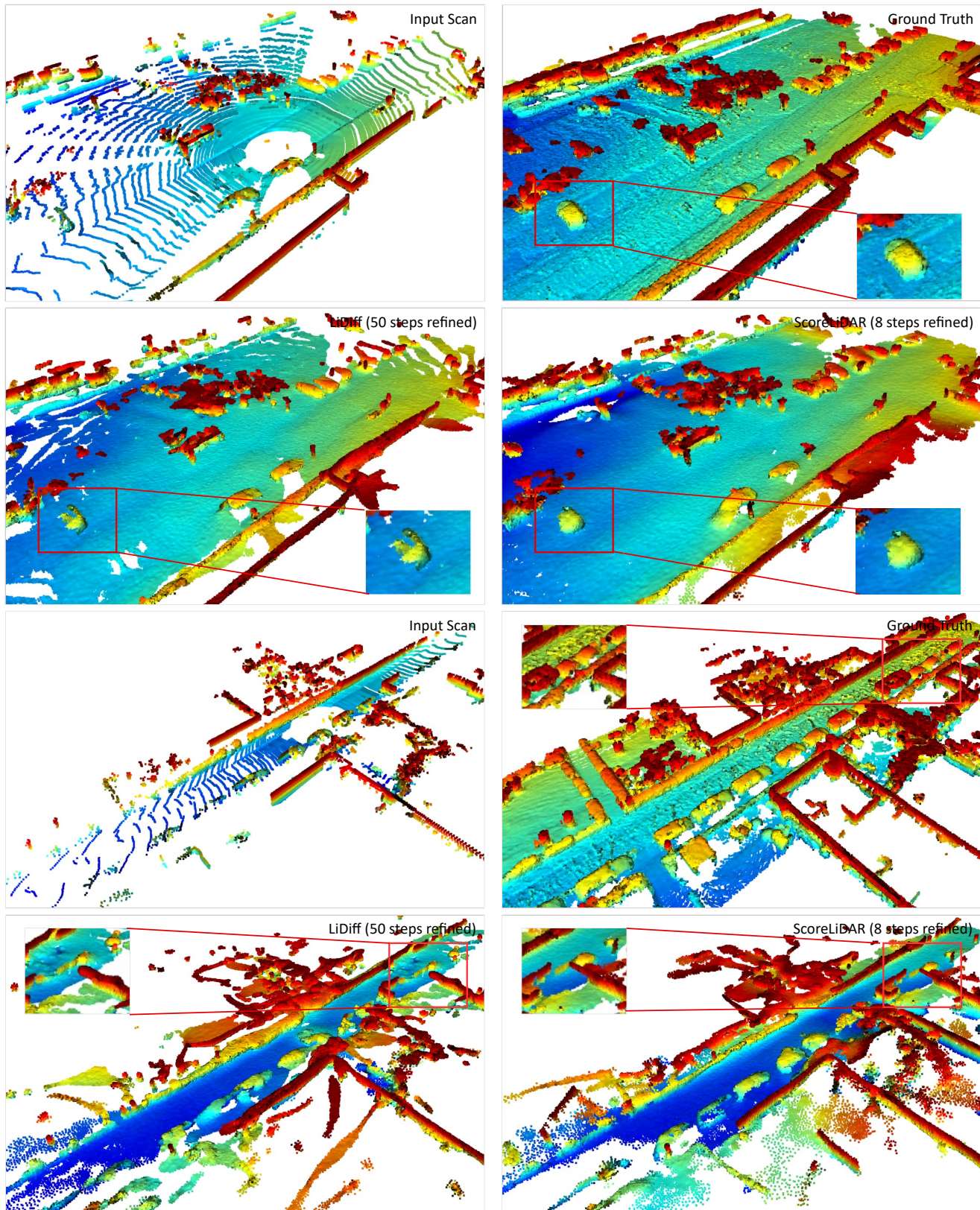


Figure 8. Completed samples of ScoreLiDAR from SemanticKITTI dataset.

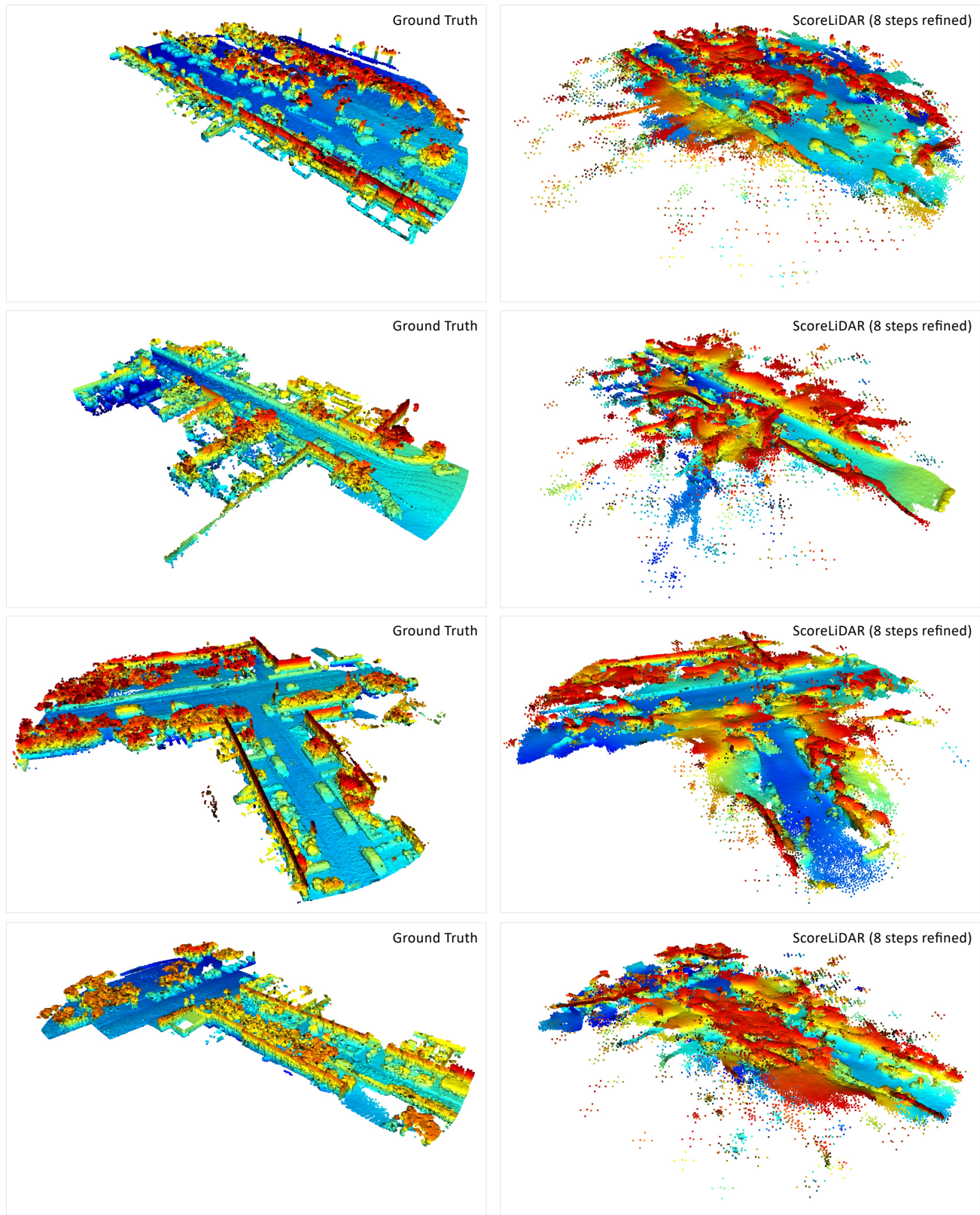


Figure 9. Failure examples of ScoreLiDAR.